

Convection-Permitting Simulations with the E3SM Global Atmosphere Model

P. M. Caldwell¹, C. R. Terai¹, B. Hillman², N. D. Keen³, P. Bogenschutz¹, W. Lin⁴, H. Beydoun¹, M. Taylor², L. Bertagna², A. Bradley², T. C. Clevenger², A. S. Donahue¹, C. Eldred², J. Foucar², C. Golaz¹, O. Guba², R. Jacob⁵, J. Johnson⁶, J. Krishna⁵, W. Liu⁷, K. Pressel⁸, A. G. Salinger², B. Singh⁸, A. Steyer², P. Ullrich⁷, D. Wu⁵, X. Yuan⁵, J. Shpund⁸, H.-Y. Ma¹, C. S. Zender⁹

¹Lawrence Livermore National Lab, Livermore, CA, USA

²Sandia National Lab, Albuquerque, NM, USA

³Lawrence Berkeley National Lab, Berkeley, CA, USA

⁴Brookhaven National Lab, Upton, NY, USA

⁵Argonne National Lab, Lemont, IL, USA

⁶Cohere Consulting LLC, Seattle, WA, USA

⁷Department of Land, Air, and Water Resources, University of California-Davis, Davis, CA, USA

⁸Pacific Northwest National Lab, Richland, WA, USA

⁹Departments of Earth System Science and Computer Science, University of California, Irvine, USA

Key Points:

- Describes the Simple Cloud-Resolving E3SM Atmosphere Model (SCREAM)
- SCREAM performs well in a 40 day boreal winter simulation at 3.25 km Δx
- Resolving deep convection solves many long-standing biases in general circulation models

Corresponding author: Peter Caldwell, caldwell119@llnl.gov

Abstract

This paper describes the first implementation of the $\Delta x = 3.25$ km version of the Energy Exascale Earth System Model (E3SM) global atmosphere model and its behavior in a 40 day prescribed-sea-surface-temperature simulation (Jan 20-Feb 28, 2020). This simulation was performed as part of the DYnamics of the Atmospheric general circulation Modeled On Non-hydrostatic Domains (DYAMOND) phase 2 model intercomparison. Effective resolution is found to be $\sim 6\times$ the horizontal grid resolution despite using a coarser grid for physical parameterizations. Despite this new model being in an immature and untuned state, moving to 3.25 km grid spacing solves several long-standing problems with the E3SM model. In particular, Amazon precipitation is much more realistic, the frequency of light and heavy precipitation is improved, agreement between the simulated and observed diurnal cycle of tropical precipitation is excellent, and the vertical structure of tropical convection and coastal stratocumulus look good. In addition, the new model is able to capture the frequency and structure of important weather events (e.g. hurricanes, midlatitude storms including atmospheric rivers, and cold air outbreaks). Interestingly, this model does *not* get rid of the erroneous southern branch of the intertropical convergence zone nor the tendency for strongest convection to occur over the Maritime Continent rather than the West Pacific, both of which are classic climate model biases. Several other problems with the simulation are identified, underscoring the fact that this model is a work in progress.

Plain Language Summary

This paper describes the new global 3.25 km version of the Energy Exascale Earth System Model (E3SM) atmosphere model and its behavior in a 40-day boreal winter-time simulation. In exchange for huge computational expense, this high-resolution model avoids many but not all biases common in lower-resolution models. It also captures several types of extreme weather that would simply not be resolved in lower-resolution models. Several opportunities for further development are identified.

1 Introduction

Because the processes controlling Earth’s weather and its climatology are complex and inter-related, numerical models are a critical tool for predicting future conditions. Global coverage is necessary because local behavior propagates rapidly to distant areas of the globe. Simulating the whole planet imposes severe computational challenges, however. In the past, this has typically been handled by coarsening model grid spacing until simulations became affordable on the machines of the time. As of 2020, this translated to horizontal grid spacing of $\mathcal{O}(10$ km) for weather models (which simulate days to weeks at a time) and $\mathcal{O}(100$ km) for climate models (which are typically run for centuries). These grid spacings are too coarse to capture many important atmospheric processes.

The impacts of sub-grid scale processes on model climate are instead *parameterized* based on available grid-scale quantities. Typical parameterized processes include turbulent transport and mixing, gravity-wave motions, greenhouse gas and aerosol chemistry and physics, radiative transfer, and cloud physics. Cloud parameterizations are in particular complicated yet important for accurate predictions. Vapor transport, collisions, and other physics involving micron-scale water drops or ice crystals (collectively called microphysics) are critical for predicting precipitation and future changes in cloud shading. Condensation and evaporation of clouds and resulting fractional cloudiness within a grid cell (often called macrophysics) involve larger spatial scales but are still important to parameterize in conventional models. Condensational heating in convective clouds causes narrow but intense upward vertical motions which are a primary source of vertical transport of heat, moisture, and momentum in the tropical atmosphere (Riehl &

72 Malkus, 1958). Because the microphysics and macrophysics of these intense updrafts are
73 tightly entwined with their motions, convective parameterizations tend to include their
74 own microphysics and macrophysics treatments. Inconsistency between microphysical
75 treatments for convective- versus resolved-scale motions is a large source of model bi-
76 ases (Song & Zhang, 2011; Storer et al., 2015). Convection in general has proven to be
77 particularly difficult to parameterize from quantities available on the grid scale (Randall
78 et al., 2003; Stevens & Bony, 2013) and has been implicated as a primary source of cli-
79 mate change uncertainty (Sanderson et al., 2008; Sherwood et al., 2014).

80 Another challenge posed by coarse resolution is interaction with Earth’s surface.
81 Topography is not resolved at typical global model grid spacing and in fact must be even
82 further smoothed to avoid model instability (Lauritzen et al., 2015). Because topogra-
83 phy can force air upwards until it condenses, smoothing out high mountain peaks causes
84 major problems for cloud and precipitation climatology (Giorgi & Marinucci, 1996). In-
85 sufficient surface roughness means wind stresses are also too weak over smoothed topog-
86 raphy and must be parameterized. Subgrid-scale surface heterogeneity also poses prob-
87 lems for coarse models (Prein et al., 2015). And while the focus of this paper is on sim-
88 ulations with prescribed sea surface temperature, it is worth noting that ocean eddies
89 on spatial scales <10 km play a critical role in heat transport (Maslowski et al., 2008)
90 and their parameterization has proven as problematic for ocean models as convective clouds
91 are for atmosphere models (Hewitt et al., 2020). Ocean/atmosphere interaction at convection-
92 and ocean-eddy resolving scales has not (to our knowledge) been studied but is also likely
93 to have important impacts on model behavior.

94 Because so much is lost at coarse resolution, the global atmospheric modeling com-
95 munity has long pushed towards higher resolution. Unsurprisingly, better topographic
96 resolution improves orographic precipitation, snowpack, and stream flow (Pope & Strat-
97 ton, 2002; Duffy et al., 2003; Delworth et al., 2012; Caldwell et al., 2019). Sea breeze ef-
98 fects become better captured as coastal boundaries are better resolved (Boyle & Klein,
99 2010; Love et al., 2011). Because finer grid spacing allows smaller spatial and temporal
100 scales to be resolved, higher-resolution GCMs also better capture extreme precipitation
101 events (Iorio et al., 2004; Wehner et al., 2014; Terai et al., 2018). As GCM grid spac-
102 ing falls to 25 km or less, tropical cyclones begin to be resolved (Atlas et al., 2005; Bacmeis-
103 ter et al., 2014; Wehner et al., 2014; Caldwell et al., 2019), though capturing details of
104 spatial structure requires still finer resolution (Judt et al., 2021). Some classic model prob-
105 lems are, however, relatively unaffected by reducing grid spacing to 25 km. In partic-
106 ular, increased resolution does not get rid of the erroneous southern branch of the In-
107 tertropical Convergence Zone (ITCZ) common in climate models (McClellan et al., 2011;
108 Bacmeister et al., 2014; Caldwell et al., 2019). Simulation of the Madden-Julian Oscil-
109 lation (MJO) is likewise unaffected (Jung et al., 2012; Bacmeister et al., 2014). In ad-
110 dition, precipitation improvement has been found primarily in wintertime because sum-
111 mertime convection occurs at scales too small to be resolved even in relatively high-resolution
112 GCMs (Duffy et al., 2003).

113 It is notable that these remaining deficiencies are related to convective motions which
114 are unresolved even at high GCM resolutions. Given the aforementioned difficulty of pa-
115 rameterizing convection, this situation is perhaps expected. A small number of global
116 models with grid spacing fine enough to explicitly resolve the largest convection events
117 (hereafter called global convection-permitting models or GCPMs) have also been built.
118 The number of these models has exploded recently because recent advances in comput-
119 ing have tended towards allowing more calculations to be performed in parallel rather
120 than making individual calculations faster. Conventional global simulations already ex-
121 ploit all available parallelism, so won’t run faster on these new machines. Higher hor-
122 izontal resolution is a ready source of increased parallelism, so is attractive in this new
123 computing environment. Unfortunately, smaller timesteps are needed to resolve finer spa-
124 tial scales. Thus even if all columns could be computed in parallel, a given integration

125 at finer resolution requires more timesteps and therefore has a longer time-to-solution.
126 As a result, GCPM simulations can't be run as routinely nor as long as conventional global
127 models.

128 The history of GCPM modeling is nicely summarized in (Sato et al., 2019). Briefly,
129 the first GCPM was the NICAM model described in Tomita et al. (2005); Sato et al.
130 (2008, 2014). For several years its only companion was the Multiscale Modeling Frame-
131 work (MMF) described in Grabowski and Smolarkiewicz (1999), Randall et al. (2003),
132 and Grabowski (2016). The MMF isn't exactly a GCPM, however, as it replaces the phys-
133 ical parameterizations inside each grid cell of a conventional GCM with a limited-area
134 CPM. The MMF is much cheaper than a GCPM because embedded CPMs are typically
135 contained within a single computational node, avoiding MPI communication costs. Ad-
136 ditionally, the grid of the CPM is decoupled from that of the GCM, so CPMs are typ-
137 ically 2d and have domain size smaller than the GCM grid cell width. The second GCPM
138 was NASA's GOES model (Putman & Suarez, 2011), which was used as a synthetic labo-
139 ratory for designing and testing satellite campaigns (Gelaro et al., 2015) in addition to
140 more general analysis. In the last few years, enough new GCPMs have been developed
141 to warrant their own intercomparison. Called DYnamics of the Atmospheric general cir-
142 culation Modeled On Nonhydrostatic Domains (DYAMOND), this intercomparison fo-
143 cused on a 40 day simulation starting Aug 1, 2016 and included 8 models with grid spac-
144 ing less than 5 km globally. An overview of this intercomparison is presented in (Stevens
145 et al., 2019). Stevens' study shows striking agreement in outgoing longwave radiation,
146 precipitation, and precipitable water between participating models. Shortwave radiation
147 differs between models, presumably due to differences in low clouds, which aren't well
148 resolved at GCPM resolutions. Models also tend to predict a spurious peak in precip-
149 itation just south of the equator, suggesting that km-scale resolution is not the solution
150 to the double-ITCZ problem endemic to conventional climate models (Li & Xie, 2014).
151 Based on the success of this first intercomparison, a second DYAMOND intercompar-
152 ison (called DYAMOND2) is now underway. The current paper documents a new con-
153 tribution to DYAMOND2.

154 GCPMs can be viewed as a natural and beneficial extension of conventional GCMs
155 to finer resolution, but they can also be seen as the extension towards larger domains
156 of a robust research community focused on limited-area cloud-permitting models (CPMs).
157 Beginning with the explicit simulation of a single convective event (Ogura, 1963), cloud-
158 resolving simulations have steadily grown in duration and domain size. Recently, Bretherton
159 and Khairoutdinov (2015) and Narenpitak et al. (2017) describe multi-month 4 km sim-
160 ulations simulating the entire tropical channel between 45°N and 45°S. CPMs tend to
161 offer more benefit for summertime convection rather than wintertime cyclones (Prein et
162 al., 2015), as may be expected given the spatial scale of these storm types. Limited-area
163 CPM research suggests that resolution finer than 4 km is needed to resolve convective
164 ensemble statistics (Weisman et al., 1997) but finer resolution adds relatively little value
165 (Kain et al., 2008; Schwartz et al., 2009; Langhans et al., 2013). Cloud fraction tends
166 to decrease as resolution becomes finer (Prein et al., 2013; Langhans et al., 2013; Fos-
167 ser et al., 2014), a feature also found in GCPMs (Hohenegger et al., 2020).

168 A great deal of CPM research has been organized around the Global Energy and
169 Water Cycle Experiment Cloud Systems Study (GCSS). As described in a review by Krueger
170 et al. (2016), GCSS organized intercomparisons of CPMs and single-column versions of
171 GCMs for intensive observing periods spanning a wide variety of cloud regimes. These
172 intercomparisons clarified processes CPMs could and couldn't handle, often leading to
173 idealized follow-up experiments. These follow-up studies have proven invaluable for pro-
174 viding process insights and subsequent model improvements. DYAMOND is in some ways
175 the reincarnation of GCSS for the next generation of models.

176 In general, high-resolution regional studies have added value primarily by resolv-
177 ing fine-scale features rather than through upscale effects onto scales resolved by con-

178 ventional models (Prein et al., 2015; Caldwell, 2010). One potential reason for this is that
 179 lateral boundary conditions impose strong constraints on domain-averaged properties
 180 (Edman & Romps, 2014). Thus while GCPMs may be overkill for looking at fine-scale
 181 features which could be studied via limited-area models, they offer fresh new potential
 182 to solve long-standing deficiencies in the general circulation.

183 The goal of this paper is to introduce the GCPM being developed by the Energy
 184 Exascale Earth System Model (E3SM) project and to provide an initial look at its be-
 185 havior in the DYAMOND2 case study. Details about this model are provided in Section 2.
 186 Sections 3-5 describe experimental design, data for evaluation, and computational per-
 187 formance (respectively). Results in Section 6 are broken into an analysis of effective res-
 188 olution in subsection 6.1, general attributes in subsection 6.2, clouds and radiation in
 189 subsection 6.3, precipitation in subsection 6.4, and specific weather phenomena in sub-
 190 sequent subsections. Conclusions follow in Section 7.

191 2 Model Description

192 As described in Golaz et al. (2019), the E3SM project was born from the US De-
 193 partment of Energy (DOE)’s need for quantitative information about future climate for
 194 use in energy-sector decisions. Given DOE’s leadership in high-performance computing,
 195 it has been natural for E3SM to focus on compute-intensive frontiers in climate science.
 196 One of those efforts has been to develop a new GCPM called the Simple Cloud-Resolving
 197 E3SM Atmosphere Model (SCREAM).

198 Our ultimate goal is to make SCREAM as fast as possible on exascale machines
 199 by writing it in C++ using the Kokkos library (Carter-Edwards et al., 2014) for perfor-
 200 mance portability. See Bertagna et al. (2019, 2020) for a description of our design strat-
 201 egy and initial performance results. We are, however, approaching this goal by first cre-
 202 ating a prototype version in Fortran using the existing E3SM atmosphere infrastructure.
 203 This initial implementation - which is the focus of the current study - is being used as
 204 the template for the C++ implementation as well as giving us an early look at model
 205 behavior. The final implementation should be scientifically identical to this prototype
 206 version but will be much faster because of its ability to run on GPU-powered comput-
 207 ers.

208 Our strategy has been to make our first implementation as simple as possible and
 209 to start using it for science as quickly as possible. This strategy is expected to result in
 210 sub-optimal skill in our first implementation, but allows us to more rapidly produce, un-
 211 derstand, and improve our model. We believe that it is better to start with an overly-
 212 simple model and to add complexity as needed rather than to start with a more sophis-
 213 ticated/accurate model which we don’t understand.

214 Simplicity in particular means that SCREAM consists solely of nonhydrostatic fluid
 215 dynamics, a turbulence/cloud fraction scheme, a microphysics scheme, a radiation scheme,
 216 an energy fixer, and prescribed-aerosol functionality. These pieces are described in the
 217 subsections below. SCREAM does not parameterize sub-grid scale gravity-wave drag or
 218 deep convection.

219 2.1 Fluid Dynamics

220 SCREAM’s fluid-dynamics solver (hereafter dycore) solves the nonhydrostatic equa-
 221 tions of motion in a rotating reference frame with the shallow atmosphere approxima-
 222 tion and a hyperviscosity based turbulence closure. It additionally transports several con-
 223 stituents, including multiple forms of water and various aerosols. It is implemented in
 224 the High Order Method Modeling Environment (HOMME) (Dennis et al., 2005, 2012;
 225 Evans et al., 2013). HOMME contains several spectral element based dycores, includ-

ing the hydrostatic dycore used by E3SM (Rasch et al., 2019; Golaz et al., 2019; Caldwell et al., 2019) and the Community Earth System Model (Small et al., 2014; S. Zhang et al., 2020). We refer to the new nonhydrostatic dycore developed for SCREAM as HOMME-NH.

HOMME-NH uses the nonhydrostatic formulation of the equations from Taylor et al. (2020). It solves the equations in a terrain following mass based vertical coordinate (Kasahara, 1974; Laprise, 1992), with prognostic equations for the three components of the velocity field, the mass-coordinate pseudo-density, the geopotential height, and a thermodynamic variable, for which we use virtual potential temperature. The prognostic equations consist of the time-reversible adiabatic terms from Taylor et al. (2020), combined with hyperviscosity following Dennis et al. (2012) and Guba et al. (2014). For the adiabatic terms, we use a structure preserving formulation in order to preserve the discrete Hamiltonian and produce an energetically consistent model. The horizontal discretization uses the collocated mimetic spectral element method from Taylor and Fournier (2010), with conservative and monotone semi-Lagrangian tracer transport (Bradley et al., 2019). The vertical discretization uses a Lorenz staggered extension of the mimetic centered difference from Simmons and Burridge (1981). With this vertical staggering, prognostic variables are located at level midpoints, with the exception of the vertical velocity and geopotential, which are located at level interfaces. For the vertical transport terms, we use a vertically Lagrangian approach adapted from Lin (2004).

For the temporal discretization, we use a Horizontally Explicit Vertically Implicit (HEVI) approach (Satoh, 2002), discretized with an IMPLICIT-EXPLICIT (IMEX) Runge Kutta method (Ascher et al., 1997). The HEVI splitting decomposes the equations into a set of terms which represent vertically propagating acoustic waves (treated implicitly), and the remaining terms which include all horizontal derivatives (treated explicitly). We use a highly efficient IMEX method from Steyer et al. (2019) and Guba et al. (2020), with a 2nd-order accurate coupling of a high-stage high-CFL scheme for the explicit terms and a Diagonally Implicit Runge Kutta (DIRK) scheme for the implicit terms. Due to the use of the Laprise mass coordinate, the vertical acoustic waves are isolated to only two terms in the equations for vertical velocity and geopotential solved at level interfaces, leading to an implicit system for a single variable.

2.2 Model Grid

Our horizontal grid for dynamics is a cubed-sphere grid with 1024×1024 spectral elements on each face, denoted ne1024. The total number of elements is therefore 6,291,456. Within each element, fields are represented by degree-3 polynomials, using nodal values on a 4×4 grid of Gauss-Lobatto-Legendre (GLL) nodes. The edge and corner nodes are shared by adjacent elements, resulting in an average spacing between GLL nodes of ~ 3.25 km. The nonuniform spacing of GLL nodes presents some challenges to the physical parameterizations (Herrington et al., 2019), which we avoid by evaluating the parameterizations on a uniformly spaced 2×2 grid within each spectral element. This *physics grid* has $4/9$ as many physics columns as would be in a GLL-collocated physics grid. Tests show that the 2×2 physics grid provides very similar results to simulations with physics running on every GLL node (Hannah et al., 2021). Our land model is taken unchanged from E3SMv1 and is run on a $1/8^\circ$ latitude-longitude grid. Sea surface temperature in this simulation is prescribed on the high-resolution ocean grid used by Caldwell et al. (2019), which tapers from 18 km in the tropics to 6 km near the poles.

We use a relatively-fine 128 layer vertical grid with a model top at 40 km (2.25 hPa) and a sponge layer in the top 14 layers (i.e. above ~ 19 hPa). Vertical grid spacing is presented in Fig. 1. Representative grid spacing in the boundary layer is ~ 50 m, in trade Cu is ~ 100 m, and in tropical cirrus anvils is ~ 250 m.

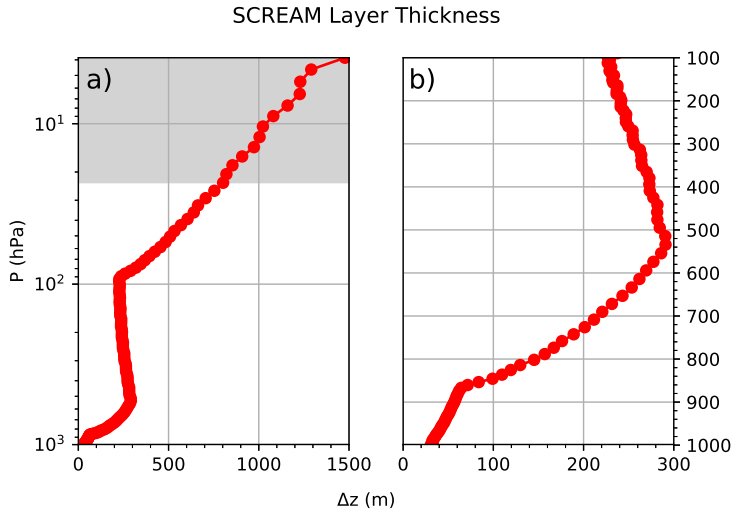


Figure 1. SCREAM grid spacing. Panel a shows the complete vertical grid using logarithmic pressure to emphasize the upper atmosphere. Panel b zooms in on the troposphere using linear pressure spacing to emphasize lower levels. The sponge layer is indicated by gray-shading.

276

2.3 Clouds and Turbulence

277

278

279

280

281

282

283

284

285

286

287

288

Boundary layer clouds and their associated circulations are still largely unresolved at 3.25 km so a parameterization of interaction between clouds and turbulence is critical. Because GCPMs push the boundary of computational possibility, it is important that these processes are handled efficiently. These goals are accomplished in SCREAM via the Simplified Higher Order Closure (SHOC; Bogenschutz & Krueger, 2013). Similar to other widely used assumed PDF-based schemes (Golaz et al., 2002; Cheng & Xu, 2008), SHOC computes subgrid-scale liquid cloud and turbulence using an assumed double-Gaussian probability density function (PDF). SHOC is more efficient than the aforementioned schemes, however, because it diagnoses rather than prognoses the higher order moments that are needed to close the double Gaussian PDF. Bogenschutz and Krueger (2013) demonstrates that SHOC is scale insensitive in limited-area cloud-resolving simulations of boundary layer clouds.

289

290

291

292

293

294

295

296

297

SHOC has undergone several updates since Bogenschutz and Krueger (2013), both to improve numerical stability and performance among the wider range of regimes SHOC is subjected to in a global model. Chief among these updates is the implementation of an implicit diffusion solver, a revised formulation of the turbulence length scale to better achieve vertical convergence, and a revised formulation of the eddy diffusivities for the stable boundary layer (similar to those implemented in Bretherton and Park (2009)). The turbulence length scale is now a continuous formulation that avoids the separate definitions of in-cloud vs sub-cloud length scales documented in Bogenschutz and Krueger (2013) and performs scientifically similarly to the original formulation.

298

299

300

301

302

303

304

305

In addition to the liquid cloud fraction supplied by SHOC, we require an ice cloud fraction. For simplicity, our initial implementation includes the same ice cloud fraction used by E3SMv1 and inherited from CESM1. This implementation assumes ice cloud starts forming when an ice-modified relative humidity $RH_i = (q_v + q_i)/q_{sat,i}$ reaches a user-specified minimum value and reaches 100% at a user-specified maximum value. Unfortunately, these parameters were left at their E3SMv1 defaults of 80% and 105% (respectively) in our DYAMOND2 simulation. The impact of this mistake is shown in Section 6.2.

306

2.4 Microphysics

307

308

309

310

311

312

313

314

315

316

317

SCREAM microphysics is based on the Predicted Particle Properties (P3) scheme of Morrison and Milbrandt (2015) taken from version 4.1 of the Weather Research and Forecasting (WRF) model (Skamarock et al., 2019). The novel feature of P3 is that it avoids arbitrary cutoffs between cloud-borne and precipitating ice categories by employing a single ice category which is allowed to evolve naturally from small pristine crystals into large and possibly rimed snowflakes. While the WRF version of P3 allows for multiple simultaneous populations of these ice crystals within a grid cell, SCREAM currently only supports a single population because the modest improvements from multiple ice populations reported in Milbrandt and Morrison (2016) were not deemed worth the additional software engineering time required to support this feature. The liquid phase of the original P3 scheme is more conventional.

318

319

320

321

322

323

324

325

326

327

328

329

330

331

One feature of this scheme is the clever use of supersaturation to diagnose condensation, evaporation, sublimation, and deposition. This approach works well for Large-Eddy simulations (LES) which explicitly model each updraft, but probably underpredicts condensation for the 3.25 km grid spacing used in SCREAM (Morrison & Grabowski, 2008). The great benefit of this supersaturation approach is that it treats ice growth at the expense of nearby liquid (Wegener, 1911; Bergeron, 1935; Findeisen, 1938, hereafter WBF process) in a very natural way. Unfortunately, allowing supersaturation in P3 directly conflicts with the instantaneous saturation adjustment assumption which forms the foundation of SHOC’s PDF. For consistency, our P3 implementation instead handles vapor deposition, sublimation, and the associated WBF process following Gettelman and Morrison (2015). In particular, maximum overlap between liquid and ice is assumed so liquid is transferred to ice by the WBF process whenever both exist. If all liquid is removed within a microphysics timestep, vapor deposition onto ice for the remainder of that timestep is computed based on cell-average water vapor content.

332

333

334

335

336

337

338

339

340

341

Another inconsistency between SHOC and the WRF version of P3 is the use of fractional cloudiness and precipitation. P3 neglected all sub-grid variability such that cloud and precipitation covered the entire grid cell where they exist and otherwise the cell was entirely devoid of condensate. SHOC provides fractional cloudiness, so we modified P3 to only operate in the cloudy or precipitating portion of each cell. Our fractional cloudiness implementation is similar to Jouan et al. (2020), which was implemented in WRF P3 around the same time as we made our modifications. The fraction of each cell containing precipitation is also important. In SCREAM this was taken to be equal to the largest cloud fraction of all cells including and above the layer of interest. This approach is crude (Zheng et al., 2020) and will be a subject of future research.

342

343

344

345

346

347

348

349

350

351

352

SHOC’s subgrid assumptions require further modifications. SHOC uses a double-Gaussian PDF to model subgrid-scale variations in liquid water potential temperature, total water mixing ratio, and vertical velocity. Larson and Griffin (2013) provide an analytical formulation for incorporating SHOC’s variability into microphysical processes expressed as power functions. We intend to implement this consistent scheme in our version of P3 eventually, but for the moment we have instead implemented the partially-consistent approach from (Morrison & Gettelman, 2008), which instead assumes a gamma distribution for liquid water mixing ratio and ignores subgrid temperature variations. The benefit of the gamma distribution is that the expected value of a power-law-based microphysical process rate can be written as that power law applied to the cell-mean value multiplied by an easily-calculated scaling factor.

353

354

355

356

357

Finally, water vapor saturation was changed in our version of P3 to be consistent with the Murphy and Koop (2005) (MK) implementation used in SHOC. MK is more accurate at very low temperatures than the (Flatau et al., 1992) implementation originally used in P3, but is more computationally expensive. We found this performance difference, however, to have a negligible impact on total run time.

358

2.5 Radiation

359

360

361

362

363

364

365

366

Gas optical properties and radiative fluxes are computed using the RTE+RRTMGP radiative transfer package (Pincus et al., 2019). Active gases in SCREAM include H₂O, CO₂, O₃, N₂O, CO, CH₄, O₂, and N₂. Cloud and aerosol optical properties are computed as in the Community Atmosphere Model (CAM). The approach is described in detail in Neale et al. (2012). Briefly, condensed phase optical properties (extinction coefficient, single scattering albedo, and asymmetry parameter for shortwave bands and absorption coefficient for longwave bands) are computed per unit mass for liquid, ice, and aerosol, then multiplied by the appropriate mass mixing ratio for use in RTE+RRTMGP.

367

368

369

370

Liquid cloud optical properties are computed from a table-lookup after being computed offline using a Mie scattering code (Wiscombe, 1996) based on the assumption (taken from microphysics) that the number of liquid drops with diameter D follows a gamma distribution

$$n(D) = N_0 D^\mu e^{-\lambda D}$$

371

372

373

374

375

376

with intercept parameter N_0 , slope parameter λ , and spectral size dispersion μ taken every timestep from P3. Ice cloud optical properties are specified in a lookup table as a function of the ice effective particle size for each shortwave and longwave band considered in the radiation code, based on the modified anomalous diffraction approximation (Mitchell, 2002). Aerosol optical properties are specified in a lookup table as a function of wet refractive index and wet surface mode radius (Ghan & Zaveri, 2007).

377

378

379

Vertical overlap of partially-cloudy cells is accounted for by assuming maximum-random overlap (Geleyn & Hollingsworth, 1979) using the Monte Carlo Independent Column approach (MCICA Pincus et al., 2003).

380

2.6 Prescribed Aerosol

381

382

383

384

385

386

387

388

389

390

E3SMv1 uses a 4 Mode Aerosol Model (MAM4 Liu et al., 2016). For computational efficiency, we employ a version where this modal aerosol information is prescribed using monthly-average climatologies interpolated to the model grid from a 1° resolution E3SMv1 simulation. Implementation and use of prescribed-aerosol functionality is described in K. Zhang et al. (2013), Lebassi-Habtezion and Caldwell (2015), and Shi and Liu (2018). The default prescribed-aerosol implementation scales aerosols by different random perturbations every day to improve agreement between prescribed- and prognostic-aerosol simulations at high latitudes. These random daily jumps are confusing for analysis of short timeseries, so we've set the magnitude of random perturbations to zero for DYAMOND2. This might degrade aerosol behavior in polar regions.

391

392

393

394

Like E3SMv1, cloud condensation nuclei (CCN) are derived from Abdul-Razzak and Ghan (2000). Ice nucleation follows Gettelman et al. (2010) for deposition nucleation and homogeneous freezing of solution droplets but retains the original P3 implementation for cloud and rain drop freezing.

395

2.7 Energy Fixer

396

397

398

399

400

401

SCREAM inherited its energy fixer from CAM. As described in Lauritzen and Williamson (2019), this energy fixer corrects errors due to pressure work, time integration in the dynamical core, inconsistent formulations of equation of state, and other minor sources of non-conservation. Historically, CAM and the atmospheric component of E3SM had used an incorrect formulation for energy. Williamson et al. (2015) documents this problem and provides a correction, which is used in SCREAM.

Main	Dycore	Dycore Remap	Advection	Radiation
75	9.375	18.75	75	300

Table 1. Timesteps used in SCREAM DYAMOND2 simulation (in sec). Processes not listed use Main timestep.

402 2.8 Timesteps

403 Like most models, SCREAM’s timestepping is a complex mixture of substepping
 404 and superstepping of individual processes. Ideally, model timesteps would be small enough
 405 that modest changes wouldn’t have a noticeable effect on model behavior. Unfortunately,
 406 climate models have not yet reached that goal (Santos et al., 2020). Thus we list the timesteps
 407 used for the DYAMOND2 simulation in Table 1.

408 2.9 Tuning

409 Tuning is important for optimal performance of any weather or climate model, but
 410 should become less important at higher resolution where more processes are explicitly
 411 resolved and therefore expressed in a more complete and physical way. Because of time
 412 constraints and a reticence to tune away problems before understanding their source, the
 413 only parameter adjustment we made was modify the lower limit of the eddy diffusivity
 414 damping timescale to get net top-of-atmosphere (TOA) radiation roughly in balance and
 415 to control surface temperatures under stable conditions at high latitudes. While success-
 416 ful in obtaining radiative balance, this tuning resulted in clouds which are too stratiform
 417 rather than convective (as described in Section 6.3). High latitude land surface temper-
 418 ature biases remain high, indicating that more tuning work is needed.

419 3 Experimental Design

420 The focus of this study is a 40 day global simulation (Jan 20-Mar 1) performed as
 421 part of the DYAMOND2 intercomparison. Our implementation follows the guidance at
 422 <https://www.esivace.eu/services/dyiamond/winter> as closely as practicable. Atmo-
 423 spheric initial conditions come from the European Center for Medium Range Weather
 424 Forecasting (ECMWF) Integrated Forecasting System (IFS) at its native 9 km grid spac-
 425 ing. Whereas some DYAMOND2 entrants are running with interactive ocean models,
 426 SCREAM is not yet able to do this. Instead we use sea surface temperature (SST) at
 427 6-hourly resolution as prescribed from IFS output smoothed by a 7 day running mean.
 428 Like most E3SM simulations, this DYAMOND2 run was performed using a no-leap-year
 429 calendar so the simulation ends Feb 28th.

430 As mentioned in Sect. 2.2.6, aerosol distributions are prescribed from a 1° E3SMv1
 431 simulation. This simulation was 6 years long with annually-repeating 2010 conditions.
 432 The last 5 years are averaged to create a monthly varying aerosol field.

433 Soil and snowpack initial conditions were computed in 2 steps. First, the E3SM
 434 land model was run from Jan 1, 1979 through Aug 1, 2016 at the target resolution forced
 435 by observed atmospheric conditions from Version 7 of the Climatic Research Unit - National
 436 Centers for Environmental Prediction (CRUNCEPv7, Viovy (2018)) atmospheric
 437 forcing data. This simulation couldn’t be extended beyond 2016 because of CRUNCEPv7
 438 data availability. The second step was therefore to run from Aug 1, 2016 to Jan 20, 2020
 439 using EAMv1 at 1° nudged to ERA5 reanalysis with a 6 hr timescale. Prescribed weekly
 440 sea surface temperature and sea ice from OISSTv2 (Reynolds et al. (2002)) is used for

441 this simulation. The machinery for this second step came from the Cloud-Associated Pa-
 442 rameterizations Testbed (Phillips et al. (2004); Ma et al. (2015)).

443 **4 Observations for Evaluation**

444 The short duration of this simulation and our focus on small time and spatial scales
 445 limit the range of observational datasets suitable for comparison. We rely heavily on the
 446 European Centre for Medium-Range Weather Forecasting’s ERA5 reanalysis (Hersbach
 447 et al., 2020). This retrospective simulation assimilates a massive array of observations,
 448 runs at 31 km horizontal resolution with 137 vertical levels and a top at 0.01 hPa, and
 449 is available at hourly resolution. Because model formulation strongly affects cloud and
 450 precipitation predictions from reanalysis, we use satellite products for cloud-related vari-
 451 ables. In particular, we use half-hourly 0.1° gridded Global Precipitation Measurement
 452 (Hou et al., 2014, GPM) Integrated Multi-satellitE Retrievals for GPM (IMERG) prod-
 453 uct (G. J. Huffman & coauthors, 2019) for global precipitation. For radiative fluxes, we
 454 use CERES-SYN hourly 1° data (Doelling et al., 2013, 2016). Cloud fraction and liq-
 455 uid water content are taken from CloudSat (Austin et al., 2009; Su et al., 2011) and from
 456 the CERES-CALIPSO-CloudSat-MODIS merged product (Kato et al., 2010, C3M). Cloud-
 457 Sat and C3M are not available for the 2020 dates simulated and are instead climatolog-
 458 ical averages.

459 **5 Performance**

460 The DYAMOND2 simulation was performed as a series of 1536-node job submis-
 461 sions using the Knights Landing (KNL) nodes of Cori at the National Energy Research
 462 Supercomputing Center (NERSC). We found that using 8 MPI processes and 16 OpenMP
 463 threads per node provided the optimal balance of memory usage and performance for
 464 these 1536-node jobs. The overall throughput for the 40-day simulation, including I/O,
 465 was about 4-5 simulated days per day (SDPD). Further details about the performance
 466 of this 40-day DYAMOND2 simulation can be explored at [https://pace.ornl.gov/
 467 search/SCREAMv0.SCREAM-DY2.ne1024pg2.20201127](https://pace.ornl.gov/search/SCREAMv0.SCREAM-DY2.ne1024pg2.20201127). The model scales quite well and
 468 has been run on up to 8192 nodes. Benchmarks of the full model without I/O and not
 469 including initialization time achieve 23.1 SDPD on 6144 KNL nodes, with the atmosphere
 470 component running at 28.4 SDPD.

471 The simulation used the Software for Caching Output and Reads for Parallel I/O
 472 (SCORPIO) library for reading input data and writing simulation output to the file sys-
 473 tem. SCORPIO is derived from the Parallel I/O library (Hartnett & Edwards, 2021) and
 474 continues to support the same application programming interface. To improve the I/O
 475 write performance the library caches and rearranges output data between MPI processes
 476 before using low level I/O libraries like the netCDF, Parallel netCDF (PnetCDF) (Latham
 477 et al., 2003), and ADIOS (Godoy et al., 2020) libraries to write the data to the file sys-
 478 tem. On Cori the simulation produced ~4.5 TB of data per simulated day and achieved
 479 an average I/O write throughput of ~2.5 GB/s using the PnetCDF library.

480 Unsurprisingly for such a large run, we experienced several node failures during the
 481 simulation requiring restarts from the previous day. Because E3SM is bit-for-bit repro-
 482 ducible for identical initial conditions and forcings, these failures should not have any
 483 impact on our results. During model development, we had problems with occasional ex-
 484 tremely cold temperatures at wintertime high latitudes. We fixed this problem by in-
 485 creasing turbulent diffusivity in stable atmospheric conditions, but this had the side ef-
 486 fect of increasing time-average warm bias in polar regions. The tuning used here balances
 487 model stability against bias.

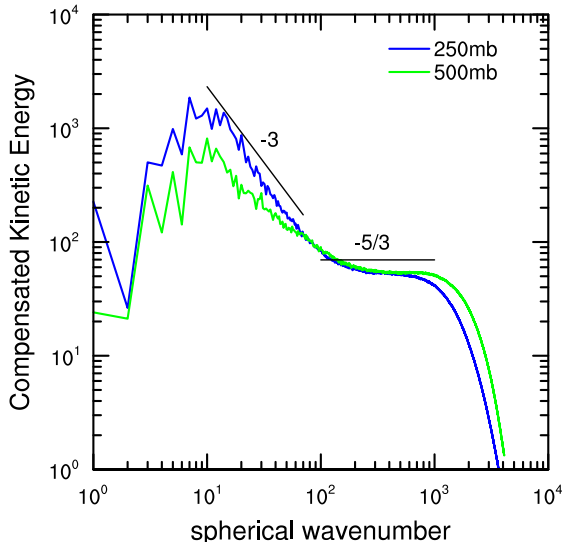


Figure 2. Compensated kinetic energy spectra ($E(k)k^{5/3}$) at 500 hPa and 250 hPa. The black lines show idealized $E(k) \approx k^{-3}$ and $E(k) \approx k^{-5/3}$ scalings.

488

6 Results

489

6.1 Kinetic Energy Spectrum

490

491

492

493

494

495

496

497

498

499

500

501

502

We plot the horizontal kinetic energy power spectra at 250 hPa and 500 hPa in Fig. 2. The spectra are computed via spherical harmonic transforms of 3-hour flow snapshots from days 22 and 23 of the simulation. We denote by $E(k)$ the power of the spherical harmonics of degree k . We plot compensated spectra, $E(k)k^{5/3}$, to better illustrate the high wave number $k^{-5/3}$ regime. SCREAM reproduces the observed Nastrom-Gage transition from a k^{-3} scaling at low wavenumbers to a $k^{-5/3}$ regime (Nastrom & Gage, 1985; Lindborg, 1999). The $k^{-5/3}$ region extends to $\sim 6\Delta x$ wavelength (wavenumber 2000), where the spectra start to roll off and become dominated by model diffusion. Thus SCREAM’s effective resolution is similar to ICON and IFS (Neumann et al., 2019) despite SCREAM’s novel use of a coarser grid for physical parameterizations. The spectra can also be influenced by model dissipation. For these runs we used a hyperviscosity coefficient of $2.5 \times 10^{10} m^4 s^{-1}$. Because tuning at 3.25 km is too expensive, we chose this value based on a Δx^3 scaling of the hyperviscosity coefficient used by E3SM at lower resolutions.

503

6.2 General Features

504

505

506

507

508

509

510

511

512

513

514

515

Global-average model biases are modest in size but are generally larger than the range of observed day-to-day variability within the simulation period (Fig. 3). TOA net shortwave (SW) radiative absorption SW_{net} and longwave (LW) emission LW_{net} are both too strong but (as noted in Section 2.9) were tuned to compensate each other such that TOA radiative bias rad_{net} exhibits only a very mild warming tendency. Radiative biases are almost entirely due to clouds rather than clear-sky bias (not shown). Too little SW_{net} reflection and excessive LW_{net} emission suggests a lack of clouds, so it is surprising that model calculated vertically-projected cloud fraction is 5% too large. This is an unfortunate result of using a RH-based ice cloud fraction parameterization without retuning for higher resolution. As a result, large cloud fraction occurs in cold regions which don’t necessarily have cloud mass (Fig. 4). Fortunately, ‘empty clouds’ like this don’t have a radiative impact, so our mistake is mostly cosmetic in nature. In the future we intend

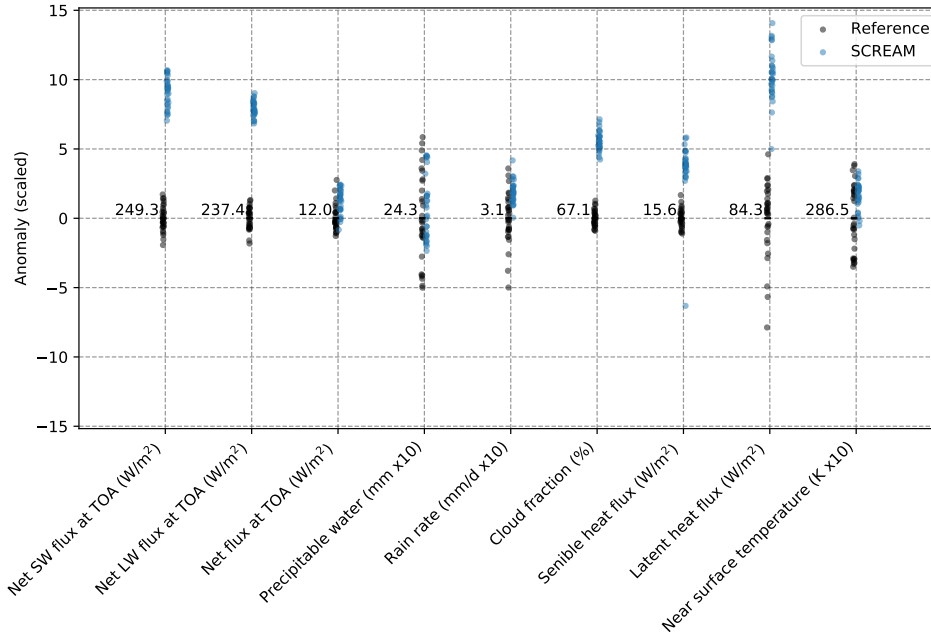


Figure 3. Global-mean anomaly in variables listed along x-axis. Anomalies are calculated relative to the long-term average of CERES-SYN (for radiative fluxes and cloud fraction), ERA5 (for precipitable water, sensible and latent heat fluxes, and near surface temperature), and GPM (for precipitation).

516 to switch to a mass-based all-or-nothing ice cloud fraction scheme to avoid this problem.
 517 An offline version of this mass-based approach is used in the remainder of this paper wher-
 518 ever upper-level cloud fraction is required.

519 Global-average precipitation is ~ 0.3 mm day $^{-1}$ larger in SCREAM than GPM, which
 520 is consistent with a general tendency for models to have higher precipitation rates than
 521 observations (Terai et al., 2018), including in the previous DYAMOND intercomparison
 522 (Stevens et al., 2019). Temperature at 2 m height (T2m) and vertically-integrated va-
 523 por lie within observed day-to-day variability in the global average, though we show later
 524 that this is due in part to compensating errors. Sensible heat flux (SHF) and surface evap-
 525 oration (a.k.a. latent heat flux; LHF) are larger than observed, probably due to near-
 526 surface wind speed biases discussed later.

527 Fig. 5 demonstrates that our simulation doesn't drift rapidly in time and captures
 528 the correct amplitude of diurnal variations. Time tendencies in other key variables are
 529 likewise small (not shown). Interestingly, SCREAM misses a couple of suppressed-precipitation
 530 periods.

531 Near-surface temperature biases are modest at low latitudes and larger at high lat-
 532 itudes (Fig. 6). In the first few days of our simulation, T2m was uniformly too high at
 533 high latitudes (not shown), which we attribute to a land initial condition created by driv-
 534 ing our land model with a 1° atmosphere model which one might expect to handle snow-
 535 pack poorly. We tuned overturning turbulent mixing in stable conditions to compensate
 536 the warm biases we saw in our initial short testing runs; it appears in retrospect that
 537 we overdid it. Averaged over the last 30 days of the simulation, the US, Greenland, and
 538 the far eastern side of Russia retain >6 K warm biases, while north Asia and the Cana-
 539 dian Arctic are ~ 5 K too cold. Improving these temperature biases is a future goal. A

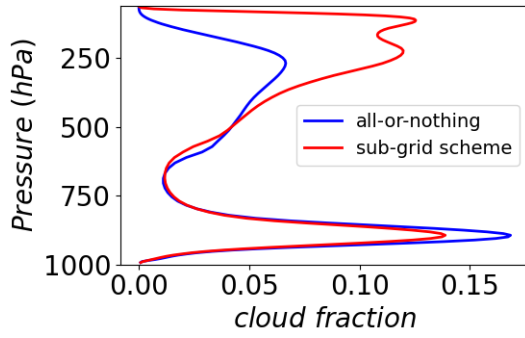


Figure 4. Vertical profile of Feb-mean tropics-averaged (30°S - 30°N) cloud fraction computed by SCREAM compared to an offline calculation of cloud fraction based on assuming an entire cell is saturated whenever cloud water content $> 10^{-5} \text{ kg kg}^{-1}$.

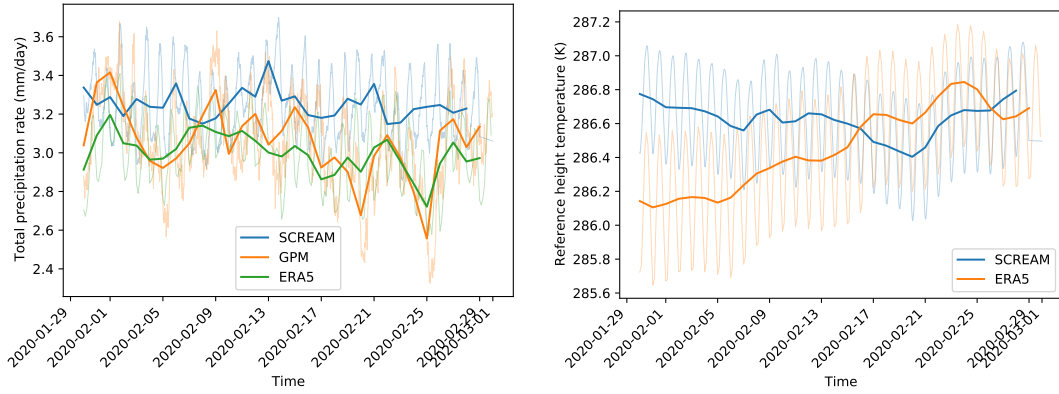


Figure 5. 15 minute (thin curves) and daily-mean (thick curves) time series of global-average precipitation (left) and T2m (right) from the last 30 days of the SCREAM simulation.

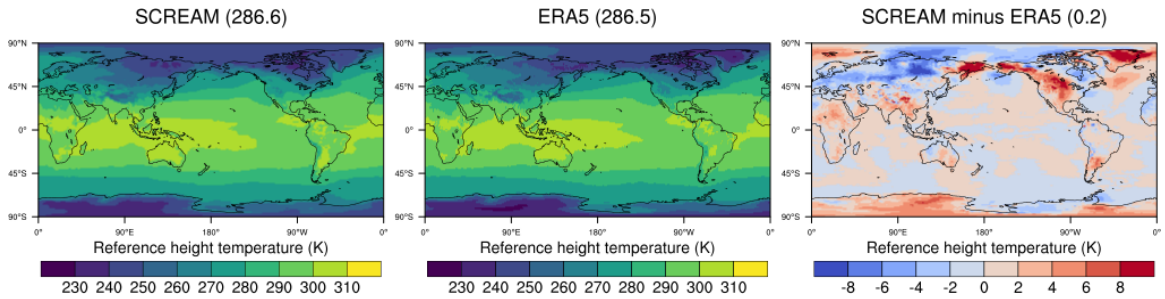


Figure 6. Near-surface temperature averaged over Feb 2020 from SCREAM and ERA5 re-analysis.

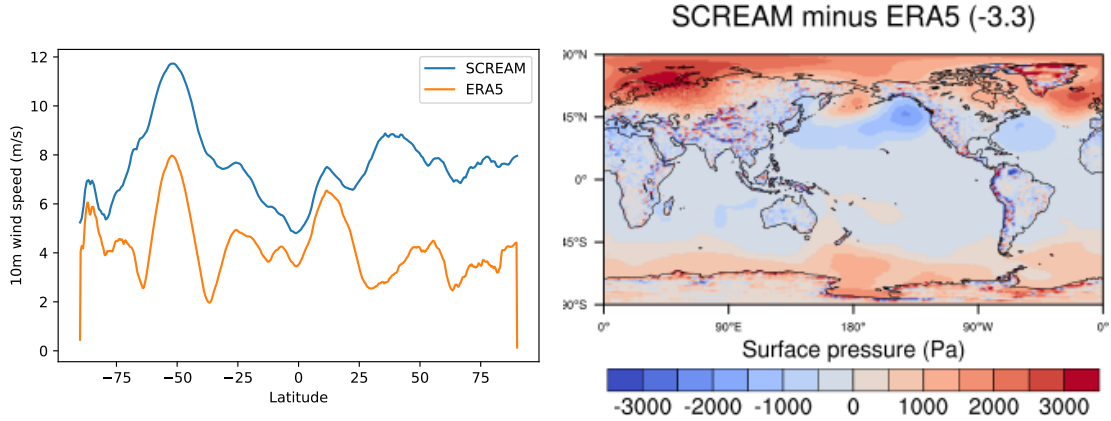


Figure 7. Zonal-average 10 m wind speed (left) and surface pressure bias (right) over the last 30 days of the simulation compared to ERA5 results for the same period.

540 byproduct of overly warm polar regions is positive surface pressure bias at high latitudes
 541 (right-hand panel of Fig. 7). This bias will translate (through thermal wind balance) to
 542 errors in wind speed.

543 Near-surface wind speed is uniformly too high (Fig. 7). Bias is smallest in the tropics
 544 and largest in the midlatitudes. This bias is the result of rushing to submit our simu-
 545 lation to the DYAMOND2 intercomparison: we should have paid more attention to tun-
 546 ing reduce near surface wind speed but didn't have time. It is surprising that so many
 547 aspects of our simulation look quite good in spite of this near-surface wind bias. Overly
 548 strong SHF and LHF mentioned earlier are unsurprising given strong near-surface wind
 549 speed.

550 Fig. 8 shows geopotential height and wind speeds on the 200hPa pressure surface
 551 averaged over the simulation period. Although there is generally strong agreement be-
 552 tween SCREAM and ERA5, two hotspots emerge. First, over North America and the
 553 North Atlantic the wintertime Rossby wave train that reinforces the upper-level trough
 554 over Greenland is markedly more intense in SCREAM than in ERA5. The result is south-
 555 ward displacement of the subtropical jet (STJ) over the West Atlantic and anomalously
 556 strong poleward flow from the STJ towards Greenland. In fact, this anomaly in the Cen-
 557 tral Atlantic is largely barotropic, present even at 850hPa with approximately the same
 558 magnitude (not shown). A second region of anomalous behavior also exists around the
 559 periphery of Australia where the 200hPa geopotential surface is enhanced, producing spu-
 560 rious meridional flow throughout this region. Notably, the bias pattern present in the
 561 difference plots suggest an enhancement in wavenumber 4 in both hemispheres centered
 562 around the locations of cubed-sphere corners in the dynamics grid. The bias appears slightly
 563 stronger in the first 20 days of the simulation than the last 20 days (not shown). The
 564 source of this behavior is under investigation.

565 6.3 Radiation and Clouds

566 SW_{net} and LW_{net} radiation biases were found in Fig. 3 to largely cancel in the global
 567 mean; Fig 9 reveals that this cancellation also holds regionally in many places. Cancel-
 568 lation between SW and LW biases is a hallmark of high clouds. Further evidence of prob-

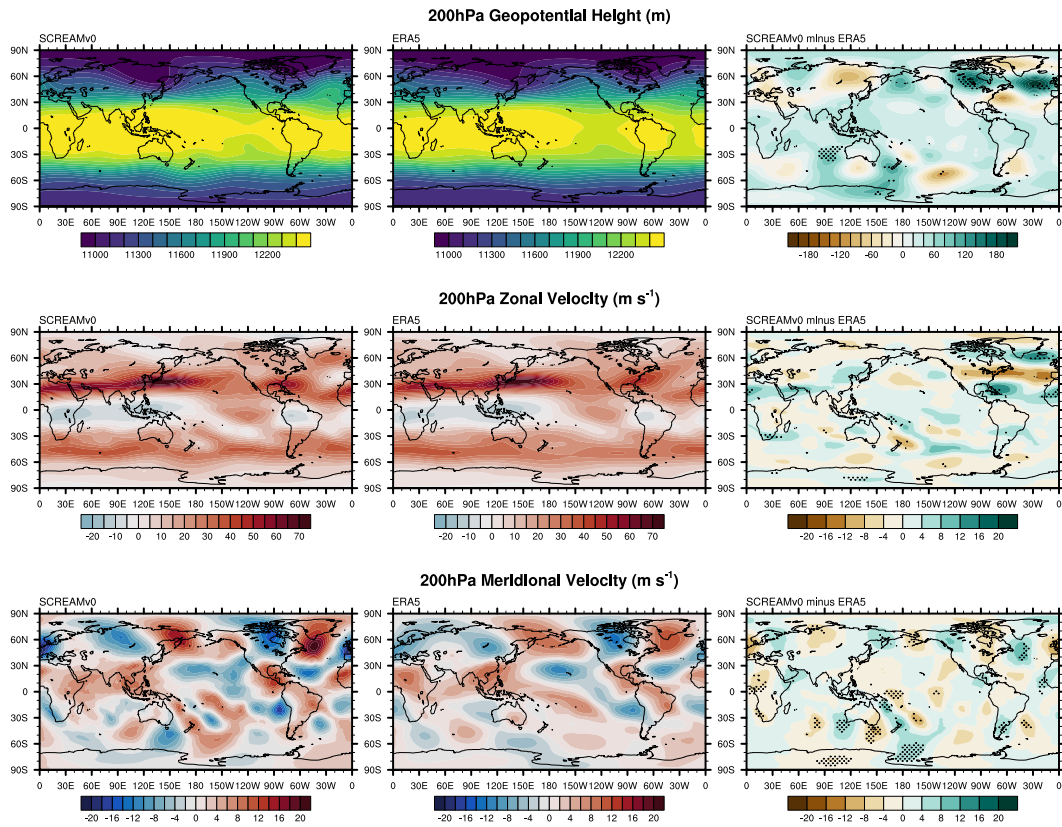


Figure 8. 200hPa geopotential height (top), zonal wind speeds (middle), and meridional wind speeds (bottom) averaged over January 20th to March 1st from SCREAM versus ERA5. Stippling in the difference plots (right panels) indicates regions where SCREAM falls outside the range of mean values for all years in ERA5 1979-2020.

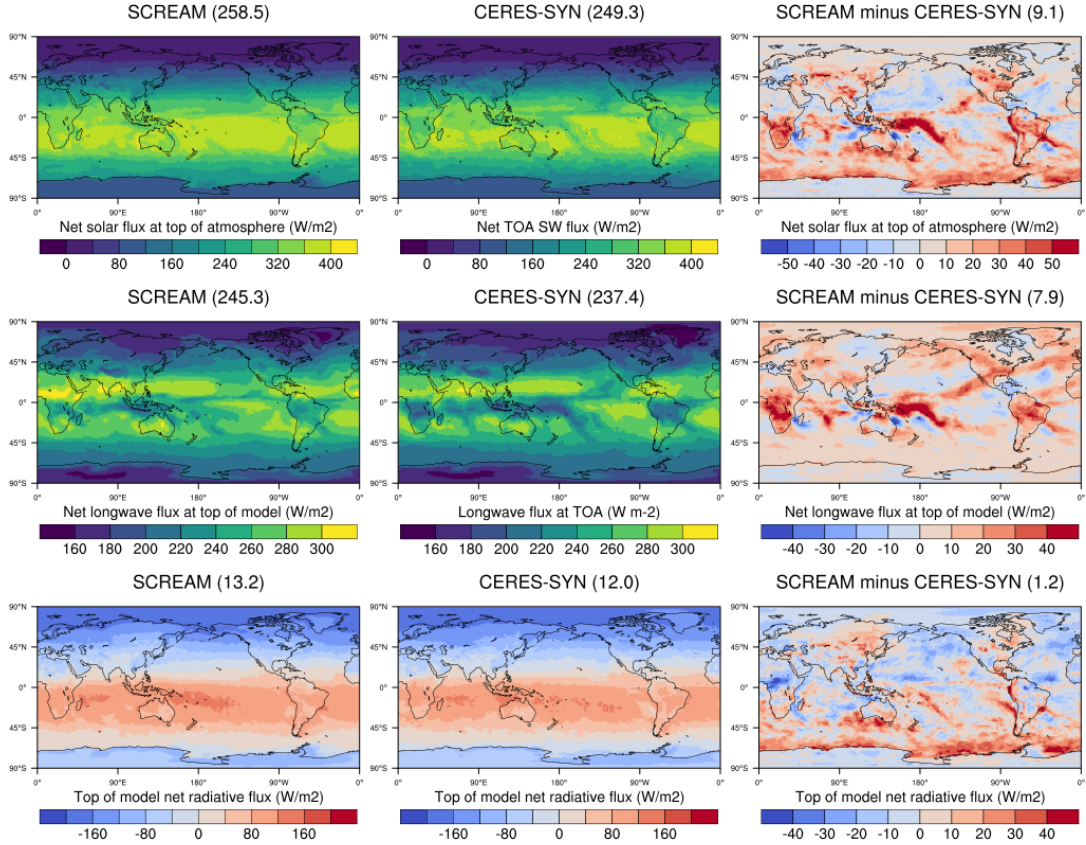


Figure 9. TOA radiation averaged over the final 30 days of the simulation. Top is SW (>0 warms the planet), middle is LW (>0 cools the planet), and bottom is net (>0 warms the planet).

569 lems with high clouds is the pattern of LW_{net} bias, which is large where deep convective clouds are expected.
570

571 Fig. 10 explores the vertical profile of tropical clouds compared to climatological
572 CloudSat measurements. Because SCREAM results are for one month only, detailed comparison
573 is not appropriate. Nonetheless, SCREAM’s ability to capture the general features
574 from CloudSat data is very good, particularly compared to the (albeit old) GCMs
575 analyzed in Su et al. (2011). In particular, SCREAM captures the bimodality of deep
576 and shallow clouds and does a reasonable job of matching the quantitative magnitude
577 of each peak. Ability to better capture the structure of tropical convection is perhaps
578 unsurprising given that resolving such convection was a primary motivation for developing
579 a 3.25 km model. Both simulated cloud peaks sit lower in the atmosphere than they do in the
580 measurements. Another notable deficiency in SCREAM is the lack of mid-level clouds, which
581 may be tied to either the absence of significant cloud detrainment at mid-levels, overly
582 efficient sedimentation of cloud particles through mid-layers, or both. Reasonable or even
583 excessive SCREAM anvil condensate in Fig. 10 and erroneously large high cloud fraction in
584 Fig. 4 are at odds with excessive LW emission to space in Fig. 9. We are still working to
585 understand this conundrum.

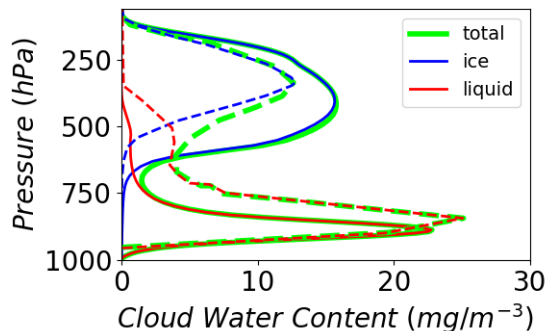


Figure 10. Cloud water content (CWC) profiles from SCREAM (solid) versus CloudSat observations from Su et al. (2011) (dashed). Data are averaged over all longitudes and latitudes between 30°S-30°N.

586 Net outgoing radiation over the northern hemisphere oceans is found in Fig. 9 to
 587 be too strong in general. This is due mainly to trapping of LW emission; SW_{net} insola-
 588 tion at higher northern latitudes is too small in wintertime to matter.

589 Away from high-latitude winter regions, the impacts of high clouds on SW_{net} and
 590 LW_{net} tend to cancel so rad_{net} is a good indicator of lower-level cloudiness. Fig. 9 re-
 591 veals a lack of low clouds over the southern ocean, but generally decent low-cloud radiative
 592 forcing in the stratocumulus decks off the west coast of the continents. Anemic strato-
 593 cumulus is a perennial GCM bias (Nam et al., 2012), so capturing this cloud type in
 594 SCREAM is a major victory. This is particularly surprising since 3.25 km grid spacing
 595 is generally considered insufficient to capture boundary-layer clouds like this. One po-
 596 tential reason for improvement is our higher-order turbulence closure. Increased verti-
 597 cal resolution (~ 50 m in the boundary layer) in addition to SCREAM’s high horizon-
 598 tal resolution also likely helps; Bogenschutz et al. (2021) and Lee et al. (2021) demon-
 599 strate that increased vertical resolution helps to ameliorate these biases in E3SM, ow-
 600 ing to better representation of the cloud top cooling and turbulence feedback, but both
 601 studies hypothesize that concurrent increases in the horizontal and vertical resolution
 602 are needed to adequately simulate the coastal Sc. Results with SCREAM support that
 603 hypothesis.

604 Figures 11a-b display the February 2020 average profiles of cloud fraction and cloud
 605 liquid water for SCREAM and the February 2006-2010 climatology from C3M. These
 606 profiles are averaged over a small domain neighboring the coast of Peru and Chile. This
 607 domain was selected as it represents the area of most intense shortwave cloud radiative
 608 effect (SWCRE) biases associated with low clouds in the boreal winter season for standard-
 609 resolution GCMs (e.g. Golaz et al. (2019); Danabasoglu et al. (2020)). Although differ-
 610 ent averaging periods are used for C3M versus SCREAM data, stratocumulus are a per-
 611 sistent feature in this region so broad comparison is reasonable. SCREAM produces cloud
 612 structure quite similar to the observations. Though SCREAM cloud fraction in Fig. 11a
 613 may appear to be underrepresented, we note that its deficiencies are small compared to
 614 most GCMs (Bogenschutz et al., 2021). In addition, cloud liquid water in Fig. 11b matches
 615 observations almost perfectly. Fig. 11c depicts a snapshot of the SWCRE on 01 March,
 616 2020 at 18:00:00 UTC for SCREAM to demonstrate the model’s ability to simulate healthy
 617 coastal Sc cloud decks and the gradual transition to more broken cloud.

618 Fig. 12 displays the temporally-averaged curtain of cloud fraction along the 20°S
 619 transect across the stratocumulus-to-deep-convection transition for SCREAM February

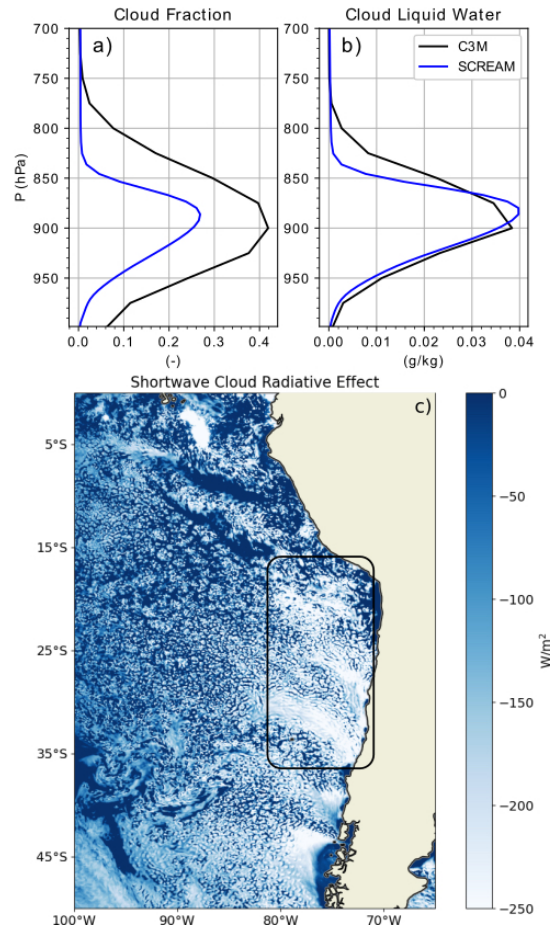


Figure 11. Temporally and spatially averaged profiles of cloud fraction (a) and cloud liquid water (b) for SCREAM and C3M. SCREAM profiles are averaged for the month of February 2020 while the C3M represents the February climatology from 2006-2010. Both SCREAM and C3M profiles represent spatial averages from the southeast Pacific coastal stratocumulus region bounded from 35°S to 15°S and 275°E to 290°E. The area used for spatial averaging is denoted in (c), which represents a snapshot of shortwave cloud radiative effect from 01 March 2020 at 18:00:00 UTC.

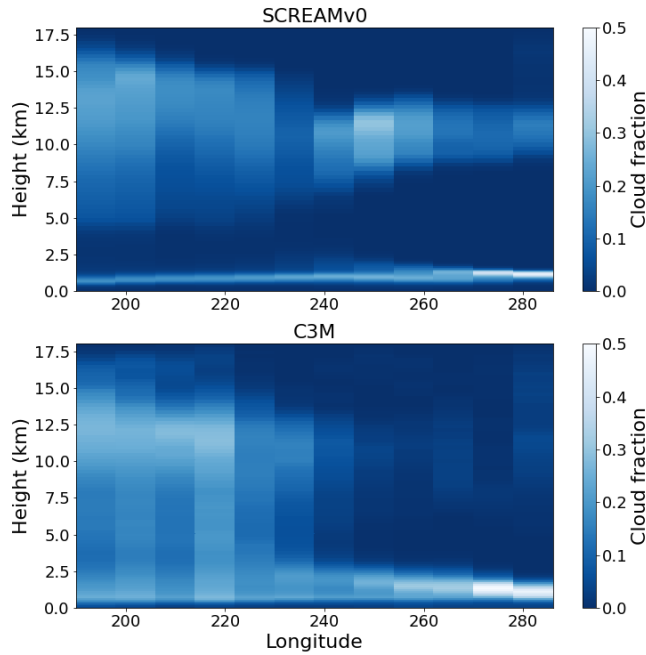


Figure 12. Temporally-averaged curtain of cloud fraction along the 20°S transect across the stratocumulus to deep convection transition. SCREAM clouds are averaged over the month of February 2020 while the C3M represents the February climatology from 2006-2010. Both SCREAM and C3M profiles represent curtains bounded from 24°S to 16°S.

620 2020 average and C3M February climatology from 2006-2010. When read from right to
 621 left (i.e. along the direction of prevailing easterly winds), C3M observations depict a grad-
 622 ual deepening of cloud in the lower troposphere over progressively warmer SSTs. SCREAM
 623 looks reasonable near the coast but fails to deepen to the W and is generally too thin
 624 in depth and too weak. We hypothesize this is an unintended consequence of tuning choices
 625 made in the SHOC parameterization to achieve reasonable radiation balance. More de-
 626 tailed tuning will be done in the future to rectify this.

627 **6.4 Precipitation**

628 Evaluating the spatial distribution of precipitation from a 40 day simulation is chal-
 629 lenging. Forty days is too long for comparison against weather events but too short to
 630 average out the effects of individual storms. Zonal-averaging beats down some of this
 631 weather noise and large-scale tropical precipitation structure is probably robust, but re-
 632 sults should still be taken with caution. In Fig. 13, zonal-average precipitation is found
 633 to generally agree well with both GPM and ERA5. Northern-hemisphere storm track
 634 structure and tropical precipitation are slightly off. Fig. 14 shows that tropical zonal-
 635 mean bias is due to a complicated mixture of differences in the meridional structure of
 636 precipitation. SCREAM tends to have stronger precipitation on the east side of land masses,
 637 in particular over the Maritime Continent (which has been a long-standing bias in E3SM;
 638 Golaz et al., 2019) and west of Madagascar. Heavy precipitation in the ITCZ extends
 639 too far east, which is another persistent E3SM bias. Precipitation in the South Pacific
 640 Convergence Zone (SPCZ) is, on the other hand, too weak and a bit too zonal. This may

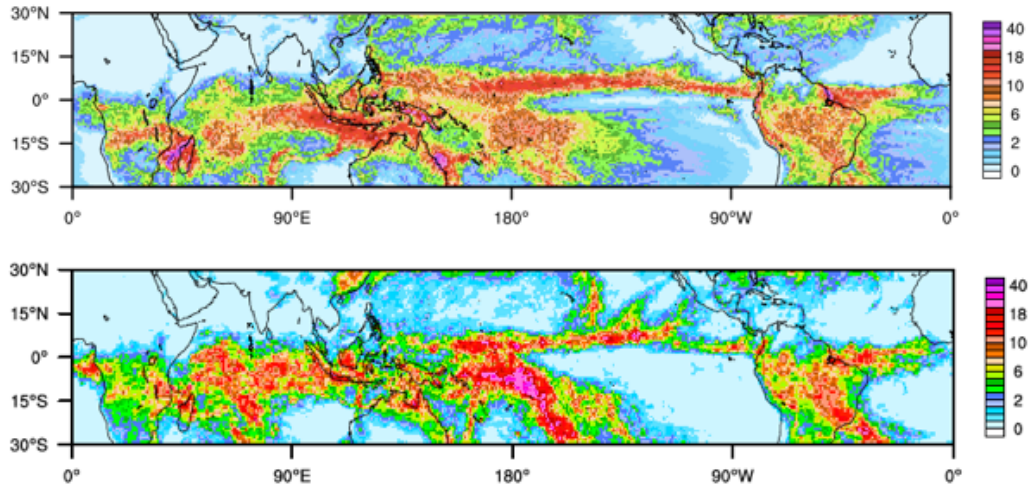
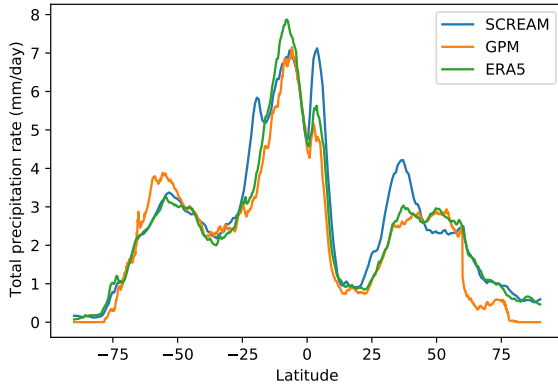


Figure 14. Tropical precipitation over the last 30 days of the SCREAM run (top) and GPM observations averaged over the same period (bottom).

641 indicate that SCREAM (like most climate models) suffers from double-ITCZ problems
 642 (Li & Xie, 2014). Precipitation over the Amazon rain forest is slightly too strong, which
 643 is the opposite from what is seen in conventional climate models (Yin et al., 2012).

644 A great success of the model is its ability to simulate the diurnal cycle of precipi-
 645 tation (Fig. 15). This is a feature which coarser resolution models struggle with (Covey
 646 et al., 2016). SCREAM is able to capture the morning-time peak over the oceans and
 647 late afternoon peak over land. The diurnal cycle over the Maritime Continent and Mada-
 648 gascar - two areas dominated by sea breezes - is actually stronger than observed in GPM
 649 (but is weaker in magnitude than TRMM’s observed climatology; not shown). Stronger
 650 diurnal amplitude in these areas is perhaps unsurprising given that daily mean precipi-
 651 tation was also noted to be too high in these regions.

652 Like conventional GCMs (Stephens et al., 2010), SCREAM has a tendency towards
 653 having too much drizzle and not enough strong precipitation (Fig. 16). The magnitude

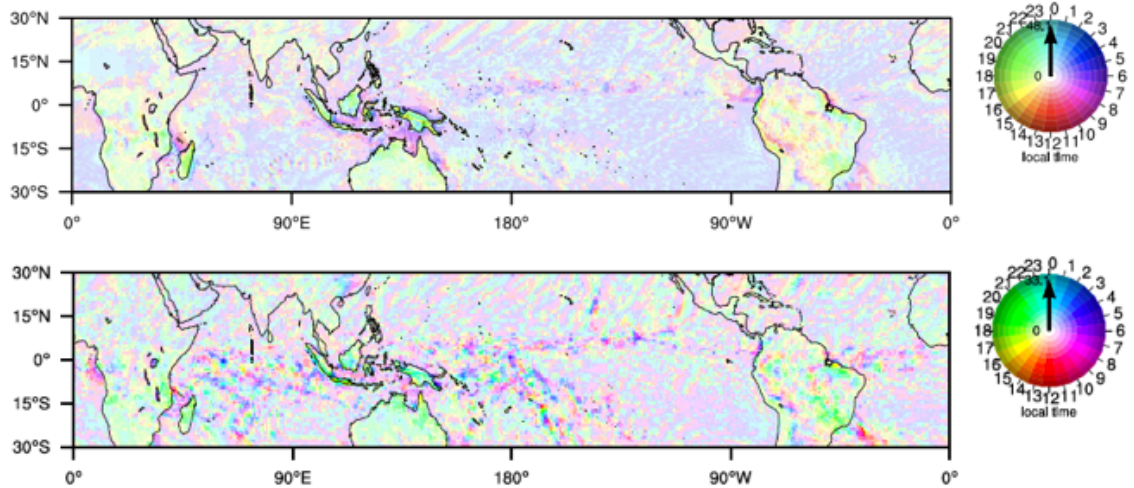


Figure 15. Diurnal cycle of precipitation in SCREAM (top) and GPM observations (bottom). Hue indicates time of peak precipitation and intensity indicates diurnal amplitude.

654 of this bias is, however, much smaller than typically found in conventional GCMs. Thus
 655 we consider simulation of heavy precipitation to be a victory for SCREAM.

656 Hovmoller diagrams showing precipitation averaged from 5° N to 5° S latitude as
 657 a function of longitude and time are useful for evaluating the temporal intermittency and
 658 propagation of tropical convection which collectively result in the Madden-Julian Oscil-
 659 lation (MJO; (Madden & Julian, 1971)). Usually MJO analyses filter out signals out-
 660 side of a 20-90 day window, but our 40 day simulation precludes such processing. A longer
 661 simulation is needed for statistical robustness, but it seems clear in Fig. 17 that SCREAM
 662 triggers convection too frequently. This feature is also apparent in instantaneous snap-
 663 shots of precipitation, water vapor, and cloud mass (not shown). We are still investigat-
 664 ing the source of this “popcorn convection”, which also appears in other convection-permitting
 665 regional and global models (Arnold et al., 2020; Kendon et al., 2012). As found for other
 666 GCPMs (Miura et al., 2007; Miyakawa et al., 2014), SCREAM does a good job of prop-
 667 agating convective events eastward.

668 The statistical analysis of precipitation above is important, but it ignores the fact
 669 that precipitation comes from storms whose characteristics vary regionally. The next few
 670 subsections explore SCREAM’s treatment of important storm types.

671 **6.5 Tropical Cyclones**

672 Tropical cyclones (TCs) are some of the most intense storms in the world, combin-
 673 ing intense precipitation with winds frequently in excess of 30 m s^{-1} . Although some global
 674 models are able to represent TC frequency and intensity well at 0.25° grid spacing, re-
 675 solving the inner structure of these storms requires much finer resolution (Wehner et al.,
 676 2014; Zarzycki & Jablonowski, 2015; Judt et al., 2021). A key advantage of running global
 677 convection-permitting models is the ability to represent and study multiscale interactions
 678 between the inner structure of tropical cyclones and the large-scale environment Satoh
 679 et al. (2019). In the first phase of the DYAMOND project, models produced a wide range
 680 of tropical cyclone counts and intensities with counts as low as 4 to as high as 20, while
 681 in reality there were 14 (Stevens et al., 2019; Judt et al., 2021). In this section, we pro-

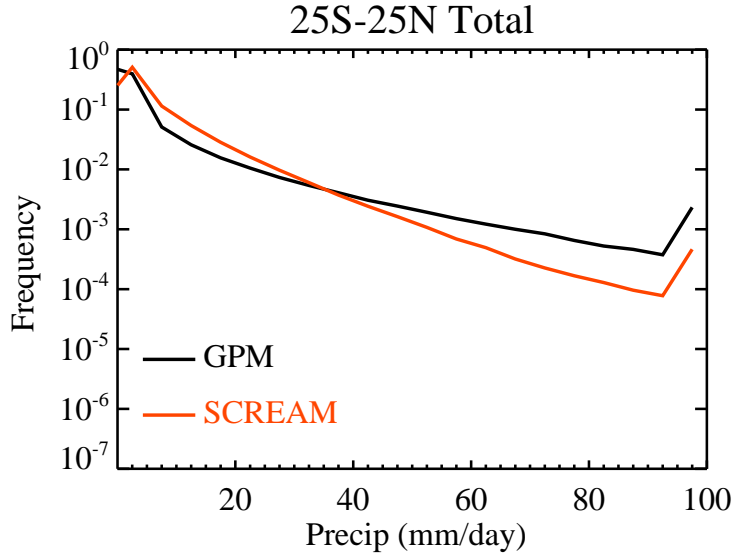


Figure 16. Histogram of tropical precipitation over the ocean from SCREAM and GPM.

682 vide a brief and broad overview of the tropical cyclones identified in the SCREAM sim-
683 ulation.

684 Using the TempestExtremes (TE) algorithm and the criteria described in appendix
685 A1, we identify five tropical cyclone tracks in SCREAM during the 40 day simulation,
686 compared to six tracks in the ERA5 reanalysis data (Fig. 18). This agreement is encour-
687 aging. All five TCs in SCREAM occur in the Southern Hemisphere, with four over the
688 Indian Ocean and one off the northwestern coast of Australia over the Pacific Ocean (Fig.
689 18), all broadly located where TCs are found in the reanalysis. Within the days of po-
690 tential predictability (up to two weeks), one TC exists in both the SCREAM simulation
691 and ERA5 data (Moderate Tropical Storm Esami). Another storm that is present in ERA5
692 in the Mozambique Channel (Moderate Tropical Storm Diane) does not organize in SCREAM,
693 although a weak low pressure region does persist.

694 In ERA5, Esami starts off as a tropical depression with central pressure of 1020
695 hPa, but whose pressure drops down to 990 hPa by Jan 26 with sustained maximum winds
696 of 25 m/s (49 knots) or more. The simulated storm track closely follows that found in
697 the reanalysis (Fig. 19a), although it forms farther to the east and moves eastward more
698 slowly. The maximum wind speed within a $6^\circ \times 6^\circ$ box around the storm is higher in
699 the model, but this is likely due to the use of native grid data in SCREAM and the coarser
700 regridding of the reanalysis data. Notably, the area-averaged precipitation rates agree
701 between SCREAM and the reanalysis, indicating that the model generally captures the
702 amount of latent heating within the storm. One discrepancy is the stronger diurnal cy-
703 cle of precipitation in the model.

704 Because Severe Tropical Storm Esami does not fully develop a canonical tropical
705 cyclone structure and exhibits hurricane force winds only for a few hours, we take a more
706 detailed look at a stronger storm in the model which forms on Feb 10 and produces sur-
707 face wind speeds which classify it as a category 3 hurricane (Fig. 19g). For reference,
708 the storm's maximum intensity (based on minimum surface pressure values) is the me-
709 dian of the five storms tracked in SCREAM (not shown). Fig. 19a shows the cyclone track,
710 which spans sixteen days. The surface pressure rapidly drops from Feb 11 to Feb 14, a
711 minimum pressure of 930 hPa on Feb 16, when maximum 10-m wind speeds are also reached.

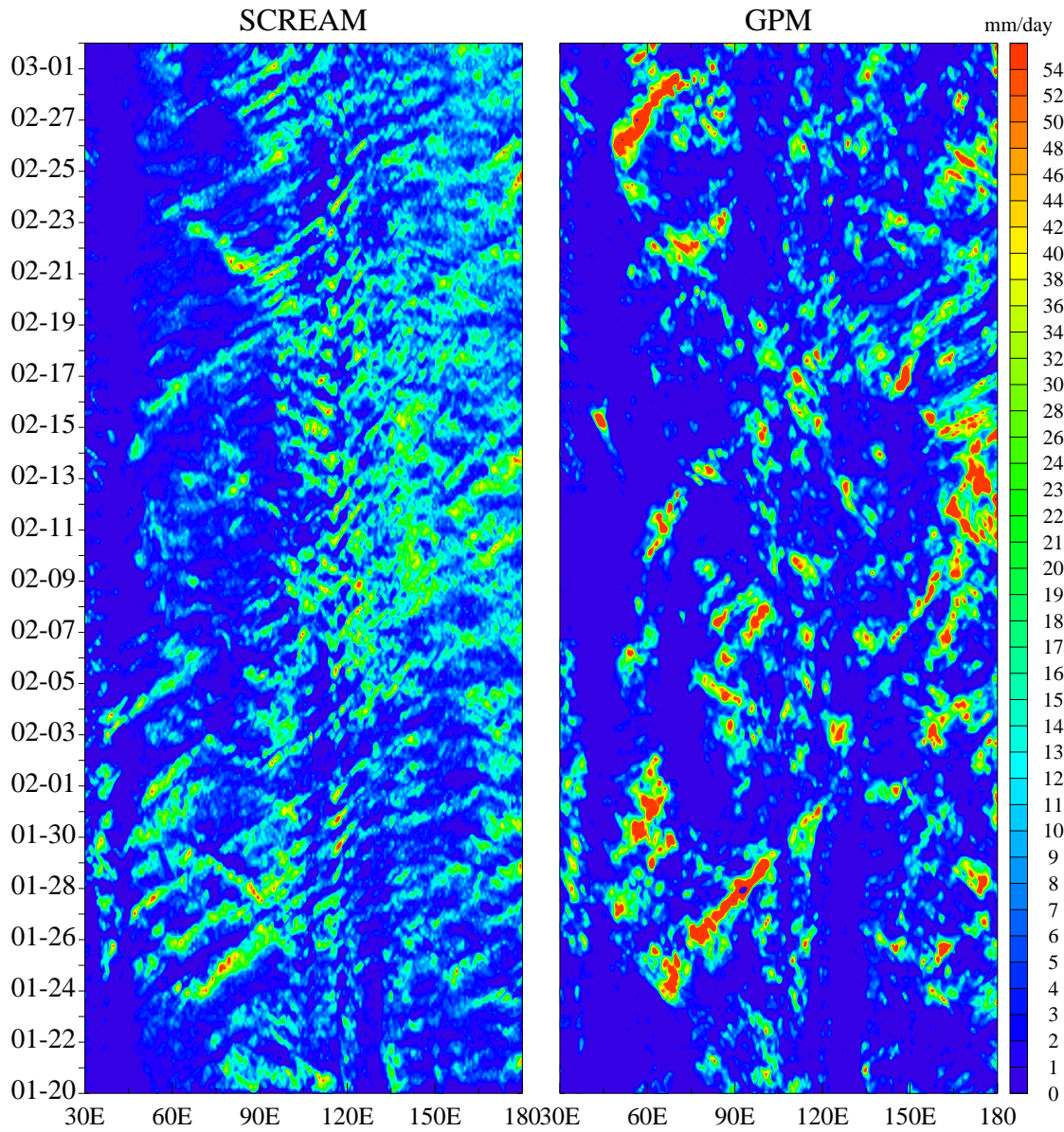


Figure 17. Precipitation averaged from 5° N to 5° S as a function of longitude (x-axis) and time (y axis) from SCREAM (left) and GPM precipitation observations (right).

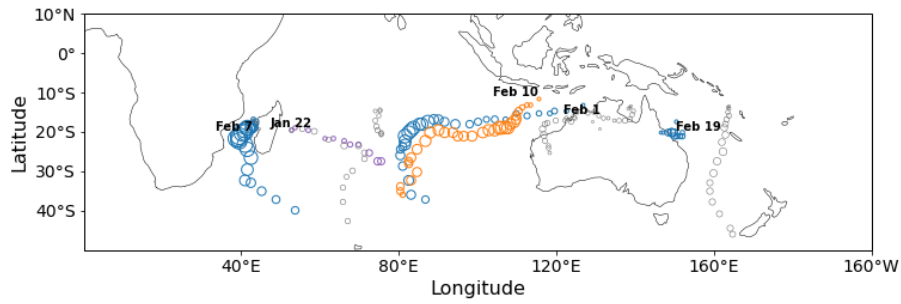


Figure 18. Tracks of tropical storms identified by the Tempest Extremes algorithm in SCREAM (blue, purple, and orange) and in ERA5 (gray) between Jan 20 and March 1, 2021. Dates indicate starting location and dates for storms identified in SCREAM.

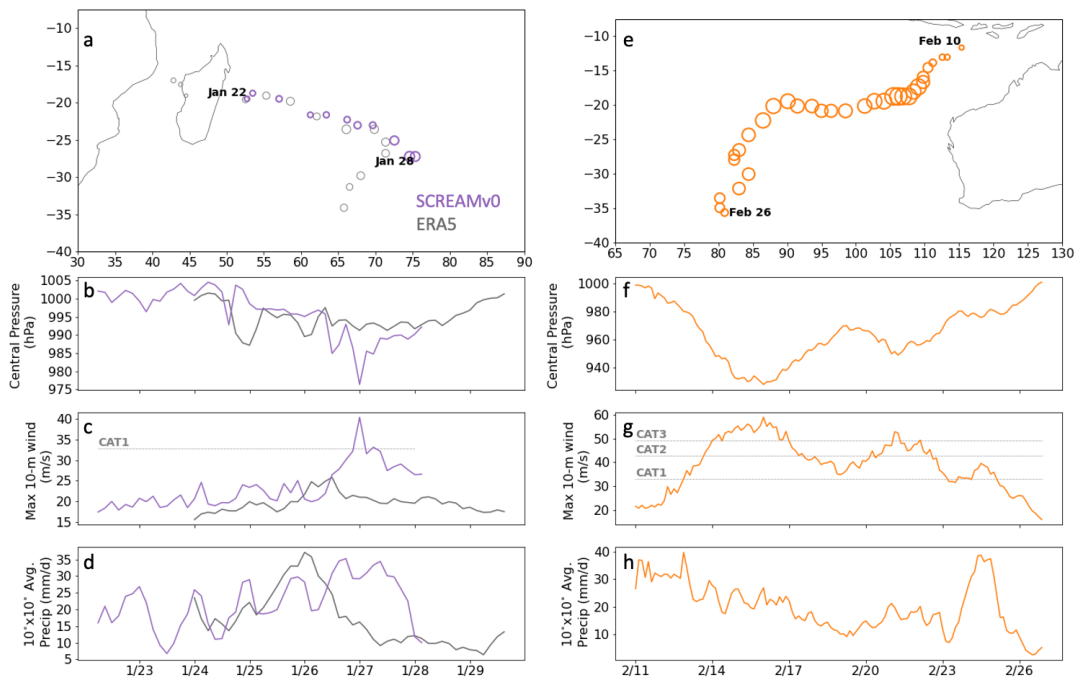


Figure 19. (a) Tracks of the tropical storm identified by the Tempest Extremes algorithm starting on Jan 22 in SCREAM (purple) and in ERA5 (gray). Shown below the tracks are time evolution of the storm's minimum central pressure (b), maximum 10-m wind speeds within 3° of the storm center (c), and area-averaged precipitation rate (d). (e-h) Same as (a-d) but for Feb 10 tropical cyclone in SCREAM simulation. No observational equivalent is shown, because it is outside the period of predictability.

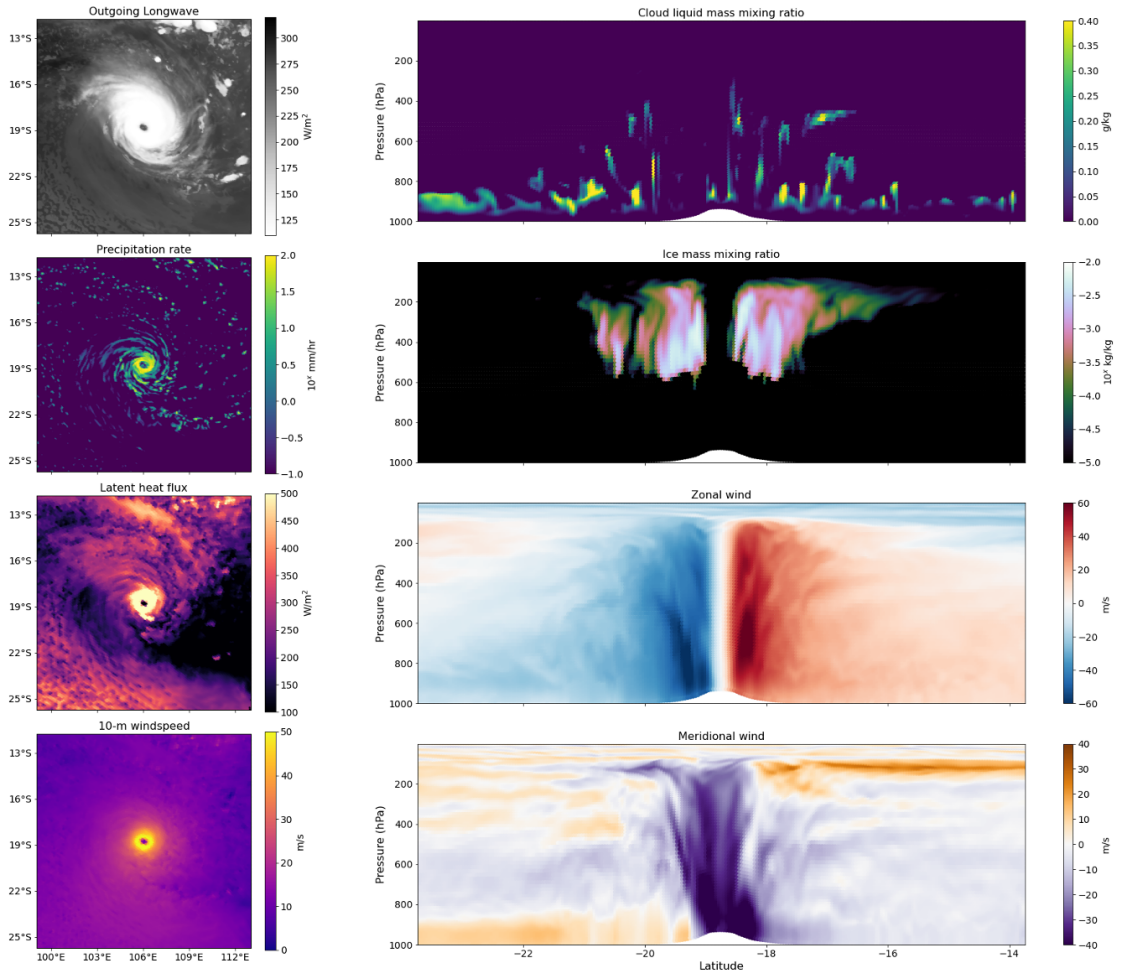


Figure 20. Instantaneous planar and curtain view of Feb 11 tropical cyclone at maximum intensity on Feb 16 00UTC. On the left column are planar views of the outgoing longwave radiation (a), precipitation rate (b), latent heat flux (c), and 10-m wind speed (d). On the right column is a north-south curtain snapshot through the center of the storm of the cloud liquid mass mixing ratio (e), ice mass mixing ratio (f), zonal wind speed (g), and meridional wind speed (h).

712 By that point, the storm has formed a distinctive eye, ringed by strong precipitation rates
 713 reaching 100 mm/hr and wind speeds greater than 60 m/s (Fig. 20). The high surface
 714 wind speeds drive surface latent heat fluxes greater than 500 W m^{-2} , and a vertical north-
 715 south curtain centered on the point of minimum surface pressure shows the boundary
 716 layer flow is transporting energy towards the eye, particularly in the southern half of the
 717 storm (Fig. 20).

718 More analysis is necessary for an in depth study of the storm characteristics in SCREAM,
 719 as was done by Judt et al. (2021) for the models participating in the first phase of DYA-
 720 MOND. However, as Fig. 19 and 20 indicate, SCREAM produces tropical cyclones with
 721 reasonable eye-wall structure and adequate surface wind intensities, which provide promise
 722 for future attempts to simulate observed tropical cyclones using the model.

723

6.6 Extratropical Cyclones

724

725

726

727

728

729

730

731

732

733

734

In mid- and high-latitude regions, extratropical cyclones (ECs) are a large source of day-to-day weather variability. ECs are a major pathway for water evaporated from the ocean to precipitate over land; Hawcroft et al. (2012) suggest that as much as 90% of the surface precipitation along midlatitude storm tracks is attributed to ECs. ECs are also behind a majority of extreme precipitation events, particularly in the northeast US where ECs are responsible for more than 80% of winter-time extreme precipitation (Pfahl & Wernli, 2012; Agel et al., 2015). With increasing resolution, ECs are better represented in global models (Jung et al., 2006), and a recent study using a set of global storm-resolving model simulations shows an increase of 7%/K in precipitation rate from the most intense extratropical cyclones with warming, which differs from the 2-3%/K increase expected in the global mean (Kodama et al., 2019).

735

736

737

738

739

740

741

742

743

744

Over the simulation time period, 87 ECs are identified in SCREAM and 80 are found in ERA5 using the TempestExtremes algorithm (see Appendix A2 for details). Their geographic distributions in the Southern and Northern Hemispheres are shown in Fig. 21a and b. In the Northern Hemisphere, the density of storms in both SCREAM and ERA5 is largest over the Atlantic and Pacific Ocean basins, with many storms originating close to the western boundary currents. This is consistent with observed climatologies of cyclone statistics (Sinclair, 1997). Bomb cyclones (ECs with surface low pressures dropping more than 24 hPa over a 24 hour period (Sanders & Gyakum, 1980)) are present in both SCREAM (11) and in ERA5 (15). While small numbers prevent us from making conclusive statements, spatial distributions in ERA5 and SCREAM seem consistent.

745

746

747

748

749

750

751

752

753

754

755

756

Fig. 21c shows the frequency of ECs by latitude band. ECs are counted separately in each 6 hourly snapshot in this plot, so counts in this plot are much higher than the ~ 80 storms quoted above for SCREAM and ERA5, which tracked single storms across time. In both hemispheres, SCREAM has a more peaked distribution with maximum frequency at the upper limit of the observed count from the 1979-2020 period. The excessively peaked EC count structure in the northern hemisphere is consistent with zonal precipitation bias shown in Fig. 13. Interestingly, modeled southern hemisphere storm track precipitation in Fig. 13 matches ERA5 almost perfectly despite having excessive EC count around 50°S . Storm composites show that Southern Hemisphere extratropical cyclones in SCREAM are associated with less rain than ERA5, which might explain this apparent paradox (not shown). Peak latitude is roughly consistent with observations in each hemisphere, though is displaced slightly poleward in the northern hemisphere.

757

758

759

760

761

762

763

764

765

766

767

768

769

770

771

772

773

774

775

We noted earlier that large swaths of the Southern Ocean in SCREAM have too much absorbed shortwave radiation compared to CERES-SYN retrievals (Fig. 9). Many climate models share biases where the cold sector of storms does not reflect enough incoming shortwave radiation, while the warm sector is less biased (Bodas-Salcedo et al., 2014). To examine whether this is the case in SCREAM, we construct composites of the cyclones tracked in SCREAM between 40°S and 60°S . This latitude band is consistent with those of Bodas-Salcedo et al. (2014), but ignores storms with centers poleward of 60°S (to remove complications due to the reflectivity of sea ice). Fig. 22 shows the composite of the pseudo-cloud albedo for SCREAM and its difference with CERES-SYN-based estimates. The pseudo-cloud albedo is defined here as the shortwave cloud radiative effect divided by the local solar insolation. By using a pseudo-cloud albedo rather than reflected shortwave radiation, we remove the potential impact of biases in the latitudinal distribution of ECs on our assessment of SCREAM's cloud reflectivity. Indeed, like the GCMs studied by Bodas-Salcedo et al. (2014), there is less cloud reflection in the cold sector of SCREAM's storms (-4.9 % in the cold western half of the storm), compared to the storms captured in ERA5. However, the warm-sector of the storm also shows lower cloud albedo (-3.8 % in the warm eastern half of the storm), showing that in SCREAM, there is a general lack of cloud reflection. Better tuning should address this problem for future simulations.

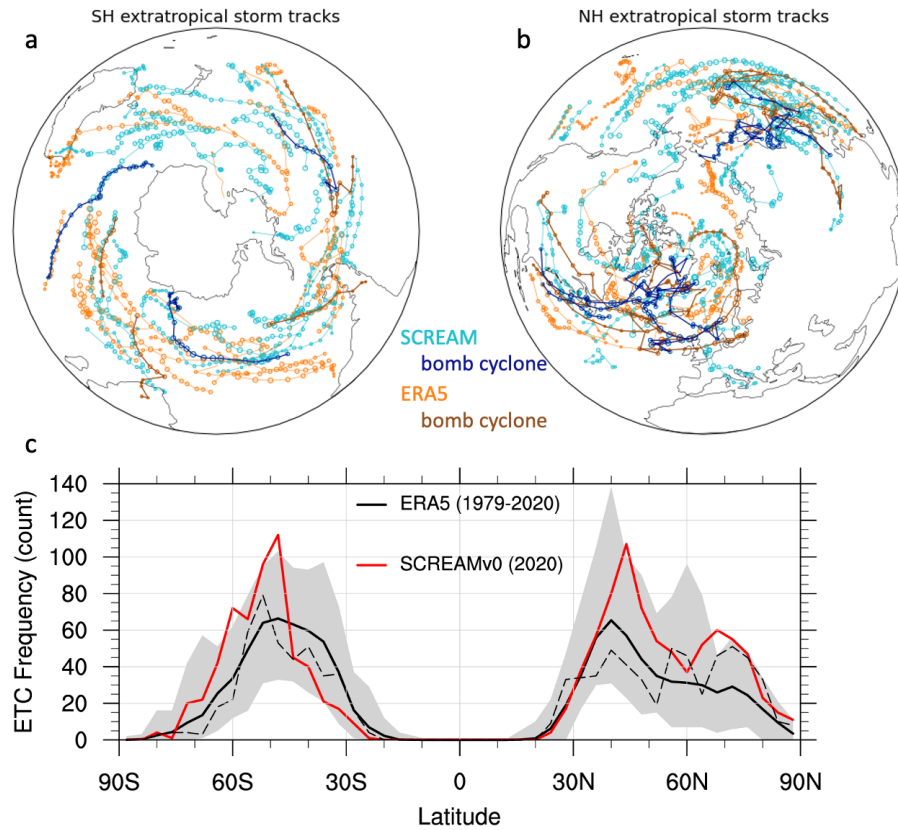


Figure 21. Geographic distribution of extratropical cyclones identified in SCREAM (cyan) and ERA5 (orange) using the TE algorithm (described in Appendix A2) for the Southern Hemisphere (a) and Northern Hemisphere (b). Dark blue tracks indicate bomb cyclones in SCREAM, whereas brown tracks indicate bomb cyclones in ERA5. (c) The latitudinal distribution of 6 hourly snapshots of extratropical cyclones in ERA5 (black) and SCREAM (red). The dashed black line indicates the distribution found in ERA5 for the DYAMOND2 period (Jan 20 to March 1, 2020). Solid black line indicates the average distribution for Jan 20 to March 1 of 1979 through 2020 in ERA5 with gray shading indicating maximum and minimum ranges for each year.

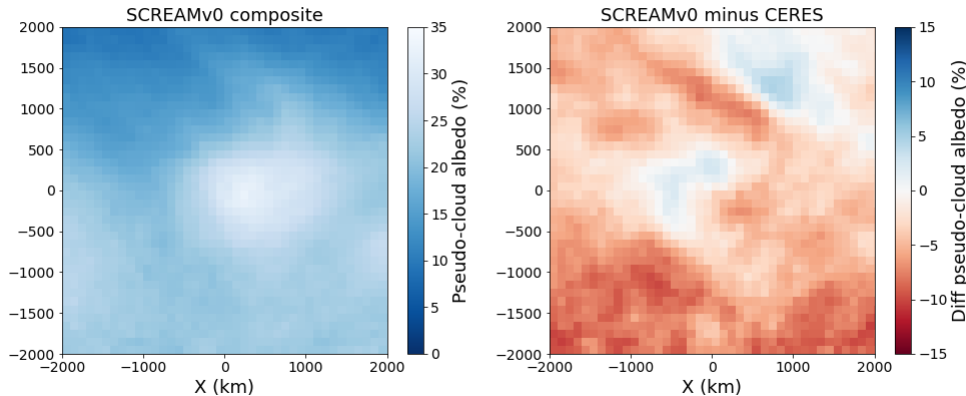


Figure 22. (left) Composite of the pseudo-cloud albedo in extratropical cyclones found between 45°S and 60°S in SCREAM. Composites average over all 6 hourly snapshots centered on identified ECs. (right) Difference in storm composite pseudo-cloud albedo between storms in SCREAM and in reanalysis and satellite data (ERA5 / CERES-SYN).

776

6.7 Atmospheric Rivers

777

778

779

780

781

782

783

784

785

Atmospheric rivers are long, narrow, and transient corridors of enhanced vapor transport typically associated with the low-level jet stream ahead of the cold front of an extratropical cyclone (AMS, 2019). As noted by Zhu and Newell (1998), atmospheric rivers are responsible for approximately 90% of poleward vapor transport. Water resources in the western U.S. are strongly tied to atmospheric rivers, with landfalling ARs providing approximately 20–50% of total wet season precipitation (Dettinger et al., 2011; Lavers & Villarini, 2015) and 30–40% of mountain snowpack (Guan et al., 2010). One such landfalling atmospheric river observed in the SCREAM simulation along the west coast of North America is depicted in Fig. 23.

786

787

788

789

790

791

792

793

794

795

796

To assess the quality of ARs in the SCREAM simulation, we track ARs over the simulation period using the TempestExtremes atmospheric river detection and tracking algorithm (McClenny et al., 2020; Ullrich & Zarzycki, 2017) as described in Appendix A3. In Fig. 24 the properties of these tracked features are then compared to analogously tracked features from all January 20th - March 1st periods in ERA5 data (1979-2020), roughly following the approach discussed in Rutz et al. (2019). In general SCREAM falls well within the climatological range from ERA5 historical simulations, except for a slight underestimation of AR frequency south of 50°S . For 2020, ERA5 predicts abnormally high AR activity while SCREAM is slightly weaker than ERA5’s long-term average. Without an ensemble of simulations to compare against, however, such a discrepancy could very easily be attributed to interannual variability.

797

798

799

800

801

802

803

804

805

806

The underestimation of AR frequency in southern high latitudes is associated with anomalously low eastward integrated vapor transport (IVT), which is in turn due to anomalously low eastward wind speeds compared to ERA5 (as highlighted in Fig. 8 and discussed in Sect. 6.2). Interestingly, Fig. 21 shows that EC frequency was actually *too high* where we find AR frequency to be too low. Perhaps ECs are spending too much time in this region due to low wind speeds? Nonetheless, the fractional contribution of ARs to poleward transport of moisture is almost identical to the climatological mean performance from ERA5, suggesting consistency of the underlying physical processes. Overall we conclude that SCREAM performs well in its representation of ARs and their associated contribution to poleward transport of vapor.



Figure 23. Snapshot of a landfalling atmospheric river along the west coast of North America that occurs on February 11th 23:00:00 UTC. Grayscale indicates vertically integrated water vapor. Colors indicate precipitation intensity.

807

6.8 Cold-Air Outbreaks

808

809

810

811

812

813

814

815

816

817

818

Marine cold air outbreaks (MCAOs) occur when cold air of polar or continental origin flow over warm ocean waters. Because of the strong air-sea temperature differences and typical higher surface wind speeds, cold air outbreaks are regions of strong surface turbulent heat fluxes that can reach 1000 W m^{-2} (Shapiro et al., 1987) and can impact frontogenesis (Terpstra et al., 2016). General circulation models (GCMs) have, however, not represented clouds under these conditions very well (Rémillard & Tselioudis, 2015). The models tend to simulate too little stratiform cloud cover in these regions (Field et al., 2014; Bodas-Salcedo et al., 2014). In this section, we describe the frequency and intensity of MCAOs in the SCREAM simulation relative to reanalysis (ERA5) during the same time period and examine the surface flux and cloud properties for a single cold air outbreak event that occurs early in the simulation over the Kuroshio current.

819

820

821

822

823

824

825

826

827

828

829

830

831

832

To identify and quantify cold air outbreaks, we use the cold air outbreak index (M) as described by Fletcher et al. (2016), which is quantified as the potential temperature difference between the surface skin and 800hPa. Any oceanic region with a positive value of M denotes a region undergoing a cold air outbreak. If we compare the frequency of cold air outbreaks in SCREAM and in ERA5 over the global oceans, we see general agreement of where and how often cold air outbreaks occur (Fig. 25a and c). Cold air outbreaks tend to occur most prominently in the winter Northern Hemisphere along the eastern edges of continents and southern edges of the sea-ice. In regions where SCREAM produces cold air outbreaks (e.g. over the Kuroshio current, Gulf stream current, and south of Alaska), M frequency tends to be higher. MCAOs are, however, greatly underestimated to the south and east of Greenland. This is unsurprising since 2-m temperature is far too warm over Greenland (Fig. 6), likely due to meridional wind biases discussed in Sect. 6.2. Except for a slight overestimation, SCREAM also tends to capture well the intensity of the strongest of cold air outbreaks (Fig. 25b and d).

833

834

835

To study the cloud fields that form under the simulated cold air outbreaks in SCREAM, we focus on a cold air outbreak event that flows off the Asian continent over the Kuroshio current from Jan 21st to Jan 22nd. We examine the cold air outbreak characteristics over

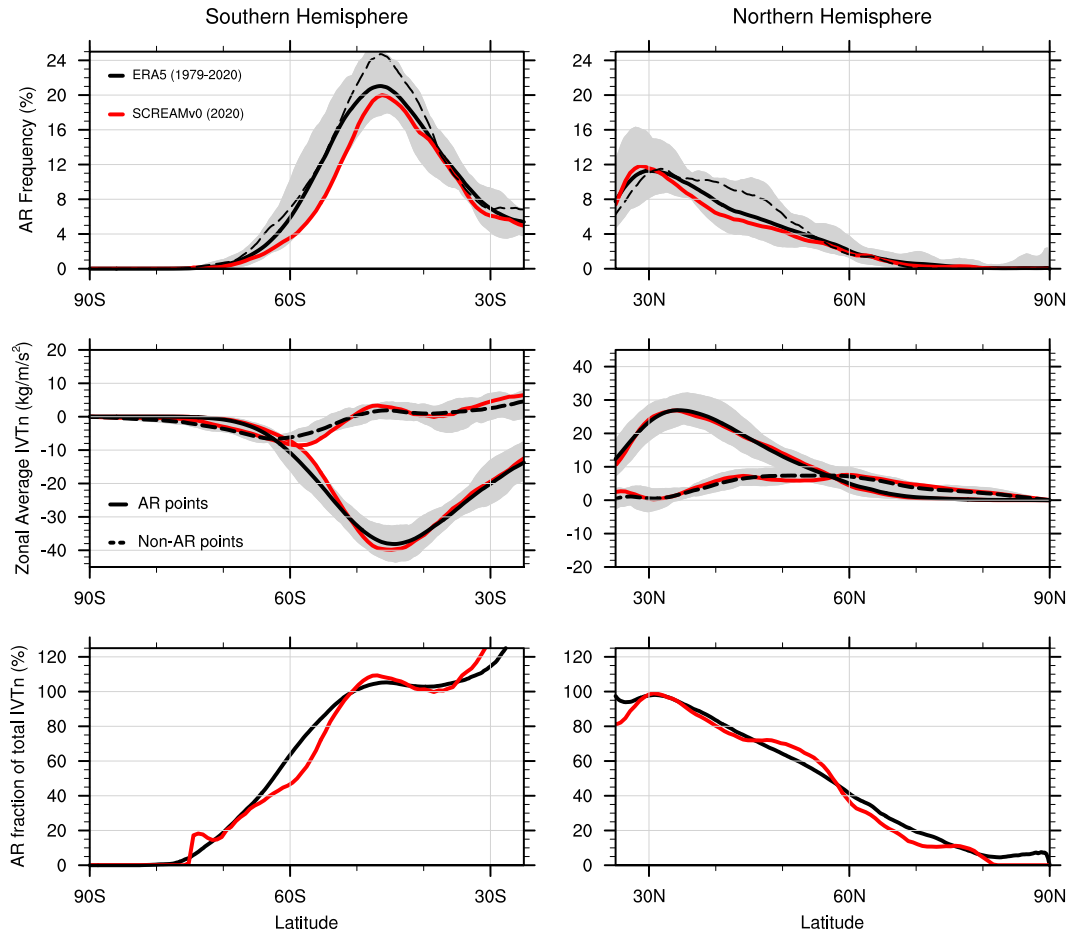


Figure 24. Properties of tracked atmospheric rivers in both hemispheres over the period January 20 through March 1 of each year in (red) the SCREAM DYAMOND2 simulation and (gray shaded region with mean shown with black solid line) 1979-2020 ERA5 reanalysis. Plots refer to (top) average atmospheric river frequency, as a percent of the full longitudinal band, with results from 2020 depicted with a black dashed line; (middle) zonally averaged northward integrated vapor transport (IVTn) at grid points flagged as part of / not part of atmospheric rivers; (bottom) mean fractional contribution of northward vapor transport from atmospheric rivers relative to all northward vapor transport.

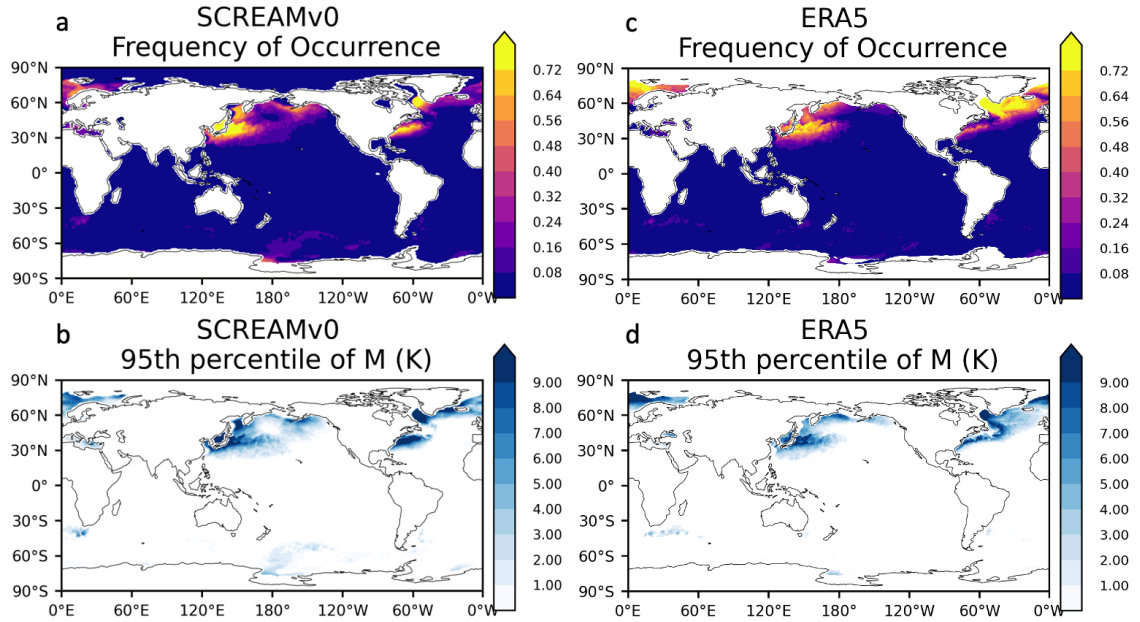


Figure 25. Frequency of cold air outbreaks (based on the M of Fletcher et al., 2016) in SCREAM over the month of February in SCREAM (a) and in ERA5 (c). Also shown is the 95th percentile value of M (including non-cold air outbreak instances) during the whole period in SCREAM (b) and ERA5 (d).

836 the 24 hour period of Jan 22nd to exclude any impacts of the cold front. The simulated
 837 sensible heat flux generally matches ERA5, but is a bit too smooth and too big (Fig. 26a
 838 and d). Good spatial agreement may be an artifact of prescribed SST; smooth features
 839 are probably due to use of a coarser (~ 6 km) ocean grid in this region. Excessive mag-
 840 nitude is unsurprising given surface wind speed biases mentioned in Sect. 6.2 and again
 841 apparent from comparing Fig. 26 panels b versus e. Surface air temperature bias does
 842 not contribute to excessive surface fluxes (not shown).

843 Although GCMs tend to underestimate the occurrence of MCAO clouds and SCREAM
 844 itself was shown earlier to suffer from a deficiency in clouds in other regimes, a compar-
 845 ison of the shortwave cloud radiative effect between the model and CERES-SYN sug-
 846 gests good agreement in the MCAO regime (Fig. 26b and d). In Fig. 27 we take a closer
 847 look at the cloud structure with a snapshot of the shortwave cloud radiative effect at 2:00
 848 UTC on Jan 22nd, which roughly corresponds to local noon time over the Kuroshio cur-
 849 rent. Closer to the continent, cloud streets form along the direction of the flow, before
 850 transitioning into broken and open-cellular convection further offshore. This prevalence
 851 of open-cellular convection in cold air outbreaks is consistent with analysis of observed
 852 cloud structures in satellite retrievals (McCoy et al., 2017). The model’s ability to cap-
 853 ture this transition suggests that SCREAM’s combination of resolution and boundary
 854 layer/cloud parameterizations contains the physics necessary to capture cloud transitions
 855 in cold air outbreaks. Further analyses compositing many cold air outbreak events would
 856 be necessary to draw more general conclusions.

857 7 Conclusions

858 The overall takeaway from this work is that 3.25 km global models solve a lot of
 859 the long-standing problems in global climate modeling even without the detailed opti-

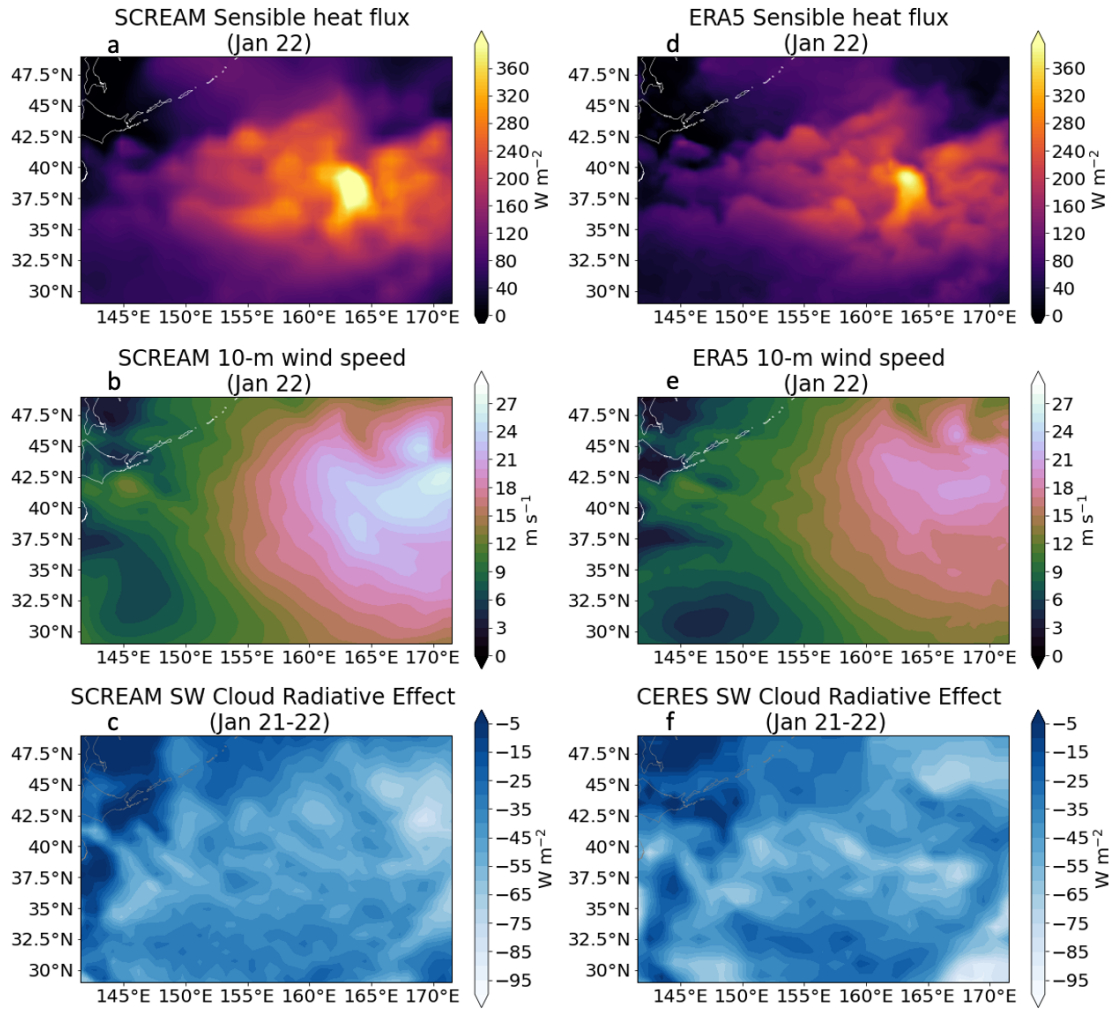


Figure 26. The daily-mean sensible heat flux over the Kuroshio region bounded from 29N to 49N and 141.5E to 171.5E in SCREAM (a) and ERA5 (d) for the cold air outbreak on January 22. Also shown are similar daily mean values of 10-m wind speed (b - SCREAM; e - ERA5) and shortwave cloud radiative effect (c - SCREAM; f - CERES-SYN).

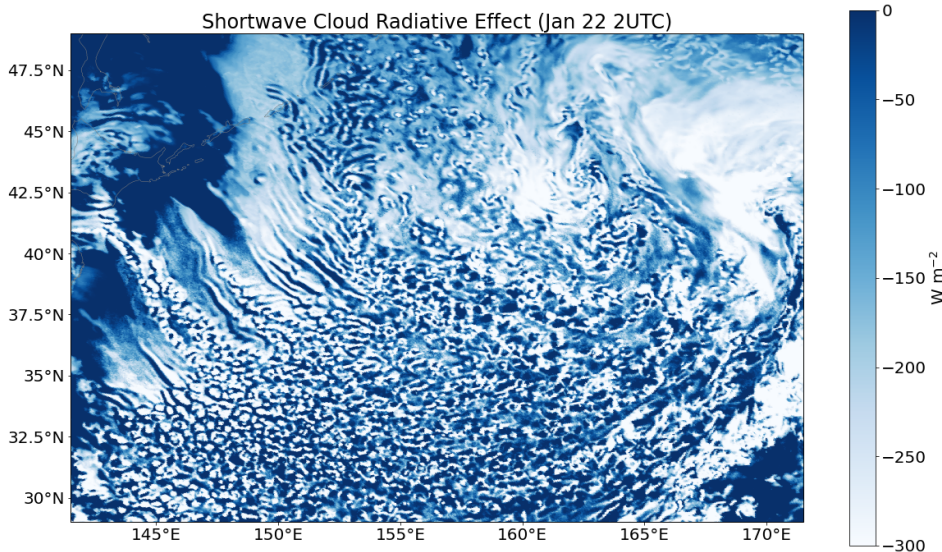


Figure 27. SCREAM-simulated instantaneous snapshot of the shortwave cloud radiative effect from 22 January 2020 at 2:00:00 UTC over a region bounded from 29N to 49N and 141.5E to 171.5E.

860 mization and tuning which is typically so important for GCM skill. In particular, SCREAM
 861 does an excellent job simulating precipitation; its diurnal cycle (Fig. 15) and intensity
 862 distribution (Fig. 16) are particularly realistic. Tropical and extratropical storm frequency
 863 and structure (Sections 6.5-6.7) are also impressive. The vertical structure of tropical con-
 864 vection (Fig. 10) is also much improved relative to typical GCMs. Coastal stratocumu-
 865 lus (Fig. 11) and cold-air outbreaks (25-27), which are perennially difficult to simulate
 866 not just in GCMs (Rémillard & Tselioudis, 2015) but also in limited-area CPMs (Klein
 867 et al., 2009), are also well captured. We suspect that the SHOC cloud/turbulence pa-
 868 rameterization and fine vertical resolution within SCREAM were important for this suc-
 869 cess.

870 Several biases in SCREAM are familiar from conventional GCMs. Clarifying whether
 871 these biases are caused by processes unresolved at 3.25 km grid spacing would be a large
 872 step towards understanding and therefore fixing these perennial problems. One such bias
 873 is the tendency for the South Pacific Convergence Zone to be too zonal (Fig. 13-14). This
 874 suggests that resolution doesn't resolve the double-ITCZ bias that plagues lower-resolution
 875 models. This finding is consistent with the result of Stevens et al. (2019) for other GCPMs.
 876 Another bias in lower-resolution versions of E3SM which persists in SCREAM is a ten-
 877 dency for precipitation in the West Pacific to be maximized over the Maritime Conti-
 878 nent rather than to the east over the ocean.

879 Analysis for this paper also revealed several deficiencies which will be fixed in fu-
 880 ture model versions. First, cloud fraction near the tropopause is corrupted by the use
 881 of a relative-humidity based ice cloud fraction scheme tuned for low resolutions (Fig. 4).
 882 Because these spurious clouds had no mass, they had little practical impact on the sim-
 883 ulation, but users of SCREAM DYAMOND2 data should be careful to use our post-facto-
 884 generated cloud-mask-based cloud fraction for future analysis. Overly strong surface wind
 885 speed is a second deficiency (Fig. 7). We suspect this results from using a surface rough-
 886 ness scaling (z_0 parameter) designed for lower resolution. Upper level winds are gener-
 887 ally reasonable but have unrealistic poleward transport north of Greenland and around

888 Australia (Fig. 8). Surface temperature at high latitudes is also problematic (Fig. 6).
 889 One potential reason for this is a land initial condition with low snowpack in mountain-
 890 ous regions exacerbated by potentially poor tuning of the lower limit on turbulent mix-
 891 ing in stable conditions and aforementioned biases related to heat transport into polar
 892 regions. Another issue is a prevalence of frequent, small "popcorn" convective events (Fig.
 893 17). Finally, cloud tuning should be improved. Shortwave reflection and longwave emis-
 894 sion are too weak (Fig. 9) and low-level clouds tend too much towards stratus and too
 895 little towards shallow convection (Fig. 12). Issues like these are expected for a new model
 896 version and most of these issues have an obvious solution. We are releasing this initial
 897 model without fixing these problems to match the timing of the DYAMOND2 intercom-
 898 parison, because there will *always* be something else to fix, and because using a model
 899 for science and writing papers is by far the fastest way to find problems.

900 This simulation is a milestone rather than an endpoint in SCREAM development.
 901 In addition to fixing the issues identified above, the major focus of the SCREAM project
 902 is on completing the computationally-performant C++ implementation of the model.
 903 We hope to perform longer, more realistic simulations soon.

904 Appendix A Feature tracking with TempestExtremes

905 For feature tracking in the DYAMOND2 simulation we use TempestExtremes 2.1
 906 (Ullrich & Zarzycki, 2017), available from ZENODO at [http://dx.doi.org/10.5281/](http://dx.doi.org/10.5281/zenodo.4385656)
 907 [zenodo.4385656](https://github.com/ClimateGlobalChange/tempestextremes) and GitHub at <https://github.com/ClimateGlobalChange/tempestextremes>.
 908 The exact commands employed in this analysis are provided in this section for reference.

909 A1 Tropical Cyclones

910 Tropical cyclone tracking is performed on 6-hourly data following (Zarzycki et al.,
 911 2017). The search is performed for local minima in the sea level pressure (PSL) which
 912 are accompanied by an increase of 200 Pa over a distance of 5.5 degrees great circle dis-
 913 tance (GCD). Tropical cyclones are further defined by the presence of an upper-level warm
 914 core which is characterized by anomalous thickness in the geopotential height between
 915 500 hPa and 200 hPa. Here we require that this thickness drop by 6.0 meters over a dis-
 916 tance of 6.5 degrees GCD, where the maxima in the layer thickness must be within 1.0
 917 degrees GCD of the pressure minima. Following this only the most intense features within
 918 6.0 degrees GCD are retained. Tracks are then stitched together in time, where sequen-
 919 tial features must be within 8.0 degrees GCD, must persist for at least 10 time steps (2.5
 920 days), can have no more than 3 sequential 6-hourly time steps where no detection is found,
 921 must have a 10 meter wind speed greater than 10 m s^{-1} for at least 10 steps along the
 922 trajectory, and must be within 50°S and 50°N for at least 10 steps along the trajectory.
 923 The commands are as follows:

```
924 $TEMPESTEXTREMESDIR/DetectNodes --in_data_list DYAMOND_TC_files.txt
925 --out DYAMOND_DN.txt --searchbymin PSL
926 --closedcontourcmd "PSL,200.0,5.5,0;_DIFF(Z200,Z500),-6.0,6.5,1.0"
927 --mergedist 6.0 --outputcmd "PSL,min,0;WINDSPD_10M,max,2" --timefilter "6hr"
928
929 $TEMPESTEXTREMESDIR/StitchNodes --in DYAMOND_DN.txt
930 --out DYAMOND_TC_tracks.txt --in_fmt "lon,lat,slp,wind" --range 8.0
931 --mintime "10" --maxgap "3"
932 --threshold "wind,>=,10.0,10;lat,<=,50.0,10;lat,>=,-50.0,10"
```

933 A2 Extratropical Cyclones

934 As with tropical cyclones, extratropical cyclone tracking is performed on 6-hourly
 935 data. Candidates are first detected as minima in the difference between the sea-level pres-
 936 sure (PSL) and the average sea-level pressure over the entire simulation (PSL_climo).
 937 We require that this difference increase by 200 Pa within 5.5 degrees GCD of the can-
 938 didate. We further eliminate points that have an upper-level warm core, as these are likely
 939 tropical cyclones, by removing candidates with a drop in the 500-200hPa layer thickness
 940 of 6.0 meters within 6.5 degrees GCD of the point of maximum layer thickness within
 941 1.0 degrees of the candidate. Following this only the most intense features within 6.0 de-
 942 grees GCD are retained. Tracks are then stitched together in time, where sequential fea-
 943 tures must be within 8.0 degrees GCD, must persist for at least 8 time steps (2.0 days),
 944 can have no more than 2 sequential 6-hourly time steps where no detection is found, must
 945 have a surface geopotential less than 700.0 for at least 8 time steps, and must have a dis-
 946 tance of 6.0 degrees GCD between genesis and termination point. The commands for these
 947 operations are as follows:

```
948 $TEMPESTEXTREMESDIR/bin/DetectNodes --in_data_list DYAMOND_ETC_files.txt
949 --out DYAMOND_DN_ETCs.txt --searchbymin "_DIFF(PSL,PSL_climo)" --timefilter "6hr"
950 --closedcontourcmd "_DIFF(PSL,PSL_climo),200.0,5.5,0"
951 --noclosedcontourcmd "_DIFF(Z200,Z500),-6.0,6.5,1.0" --mergedist 6.0
952 --outputcmd "PSL,min,0;_DIFF(PSL,PSL_climo),min,0;WINDSPD_10M,max,5;PHIS,min,0"
953
954 $TEMPESTEXTREMESDIR/bin/StitchNodes --in DYAMOND_DN_ETCs.txt
955 --out DYAMOND_ETC_tracks.txt --in_fmt "lon,lat,psl,pslanom,wind,phis" --range 8.0
956 --mintime "8" --maxgap "2" --min_endpoint_dist 6.0 --threshold "phis,<=,700,8"
```

957 A3 Atmospheric Rivers

958 Atmospheric river tracking is performed using the tracker employed in (McClenny
 959 et al., 2020). Grid points poleward of 15 degrees N/S are flagged where the Laplacian
 960 of the integrated vapor transport (evaluated using 8 points with radius 10 degrees GCD)
 961 is less than $20000 \text{ kg m}^{-1} \text{ s}^{-1} \text{ rad}^{-2}$. Only contiguous regions with area greater than
 962 $4 \times 10^5 \text{ km}^2$ are retained in this operation. Since high IVT blobs can include tropical
 963 cyclones, we also remove all points within 10 degrees GCD of TCs detected using the
 964 method described in section A1. The commands for these operations are as follows:

```
965 $TEMPESTEXTREMESDIR/DetectBlobs --in_data CAT_TUQ,TVQ_256x512.eam.nc
966 --out CAT_ARs_256x512.eam.nc --minabslat 15 --geofiltercmd "area,>=,4e5km2"
967 --thresholdcmd "_LAPLACIAN{8,10}(_VECMAG(TUQ,TVQ)),<=,-20000,0"
968
969 $TEMPESTEXTREMESDIR/NodeFileFilter --in_nodefile DYAMOND_TC_tracks.txt
970 --in_fmt "lon,lat" --in_data CAT_ARTag_256x512.eam.nc
971 --out_data CAT_ARTag_TCfiltered_256x512.eam.nc --var "binary_tag"
972 --bydist 10.0 --invert
```

973 Acknowledgments

974 This research was supported as part of the Energy Exascale Earth System Model
 975 (E3SM) project, funded by the U.S. Department of Energy, Office of Science, Office of
 976 Biological and Environmental Research. It used resources of the National Energy Re-
 977 search Scientific Computing Center (NERSC), a U.S. Department of Energy Office of
 978 Science User Facility located at Lawrence Berkeley National Laboratory, operated un-
 979 der Contract No. DE-AC02-05CH11231. This research also used resources from the Ar-
 980 gonne Leadership Computing Facility at Argonne National Laboratory, which is supported

981 by the Office of Science of the U.S. Department of Energy under contract DE-AC02-06CH11357.
 982 This paper was prepared by LLNL under Contract DE-AC52-07NA27344. H.-Y. Ma is
 983 funded by the Regional and Global Model Analysis program area and Atmospheric Sys-
 984 tem Research program of the U.S. Department of Energy. Sandia National Laborato-
 985 ries is a multimission laboratory managed and operated by National Technology and En-
 986 gineering Solutions of Sandia, LLC, a wholly owned subsidiary of Honeywell International
 987 Inc., for the U.S. Department of Energy’s National Nuclear Security Administration un-
 988 der contract DE-NA0003525. This paper describes objective technical results and anal-
 989 ysis. Any subjective views or opinions that might be expressed in the paper do not nec-
 990 essarily represent the views of the U.S. Department of Energy or the United States Gov-
 991 ernment. The SCREAM output described in this paper is publicly available as part of
 992 the DYAMOND2 intercomparison as described at [https://www.esiwace.eu/services/](https://www.esiwace.eu/services/dyiamond)
 993 [dyiamond](https://www.esiwace.eu/services/dyiamond). The GPM dataset used in this study is from G. Huffman et al. (2019) and can
 994 be accessed at https://disc.gsfc.nasa.gov/datasets/GPM_3IMERGHH_06/summary.
 995 We acknowledge and thank Jingyu Wang for accessing, formatting, and making the data
 996 available to us. The version of CERES SYN1deg data used here is Edition 4.1 with a
 997 release date of August 22, 2019 and was accessed from: [https://ceres-tool.larc.nasa](https://ceres-tool.larc.nasa.gov/ord-tool/jsp/SYN1degEd41Selection.jsp)
 998 [.gov/ord-tool/jsp/SYN1degEd41Selection.jsp](https://ceres-tool.larc.nasa.gov/ord-tool/jsp/SYN1degEd41Selection.jsp). The authors would also like to thank
 999 Jiwen Fan and Kai Zhang for their contributions to fixing bugs in our P3 microphysics
 1000 implementation.

1001 References

- 1002 Abdul-Razzak, H., & Ghan, S. J. (2000). A parameterization of aerosol activa-
 1003 tion: 2. multiple aerosol types. *Journal of Geophysical Research: Atmospheres*,
 1004 *105*(D5), 6837–6844. doi: <https://doi.org/10.1029/1999JD901161>
- 1005 Agel, L., Barlow, M., Qian, J.-H., Colby, F., Douglas, E., & Eichler, T. (2015).
 1006 Climatology of Daily Precipitation and Extreme Precipitation Events in the
 1007 Northeast United States. *Journal of Hydrometeorology*, *16*(6), 2537–2557. doi:
 1008 [10.1175/JHM-D-14-0147.1](https://doi.org/10.1175/JHM-D-14-0147.1)
- 1009 AMS. (2019, March). *Atmospheric river*. American Meteorological Society. Re-
 1010 trieved from http://glossary.ametsoc.org/wiki/Atmospheric_river
- 1011 Arnold, N. P., Putman, W. M., & Freitas, S. R. (2020). Impact of Resolution and
 1012 Parameterized Convection on the Diurnal Cycle of Precipitation in a Global
 1013 Nonhydrostatic Model. *Journal of the Meteorological Society of Japan. Ser. II*,
 1014 *advpub*. doi: [10.2151/jmsj.2020-066](https://doi.org/10.2151/jmsj.2020-066)
- 1015 Ascher, U. M., Ruuth, S. J., & Spiteri, R. J. (1997). Implicit-explicit Runge-Kutta
 1016 methods for time-dependent partial differential equations. *Applied Num.*
 1017 *Math.*, *25*(2-3), 151–167. doi: [10.1016/s0168-9274\(97\)00056-1](https://doi.org/10.1016/s0168-9274(97)00056-1)
- 1018 Atlas, R., Reale, O., Shen, B.-W., Lin, S.-J., Chern, J.-D., Putman, W., ...
 1019 Radakovich, J. (2005). Hurricane forecasting with the high-resolution nasa
 1020 finite volume general circulation model. *Geophysical Research Letters*, *32*(3).
 1021 doi: [10.1029/2004GL021513](https://doi.org/10.1029/2004GL021513)
- 1022 Austin, R. T., Heymsfield, A. J., & Stephens, G. L. (2009). Retrieval of ice cloud
 1023 microphysical parameters using the cloudsat millimeter-wave radar and tem-
 1024 perature. *Journal of Geophysical Research: Atmospheres*, *114*(D8). doi:
 1025 <https://doi.org/10.1029/2008JD010049>
- 1026 Bacmeister, J. T., Wehner, M. F., Neale, R. B., Gettelman, A., Hannay, C., Lau-
 1027 ritzen, P. H., ... Truesdale, J. E. (2014). Exploratory high-resolution climate
 1028 simulations using the community atmosphere model (cam). *Journal of Cli-*
 1029 *mate*, *27*(9), 3073–3099. doi: [10.1175/JCLI-D-13-00387.1](https://doi.org/10.1175/JCLI-D-13-00387.1)
- 1030 Bergeron, T. (1935). *On the physics of clouds and precipitation*. Proces Verbaux
 1031 de l’Association de Météorologie, International Union of Geodesy and Geo-
 1032 physics.
- 1033 Bertagna, L., Deakin, M., Guba, O., Sunderland, D., Bradley, A. M., Tezaur, I. K.,

- 1034 ... Salinger, A. G. (2019). Hommexx 1.0: a performance-portable atmospheric
 1035 dynamical core for the energy exascale earth system model. *Geoscientific*
 1036 *Model Development*, 12(4), 1423–1441. doi: 10.5194/gmd-12-1423-2019
- 1037 Bertagna, L., Guba, O., Taylor, M., Foucar, J., Larkin, J., Bradley, A., ... Salinger,
 1038 A. (2020). A performance-portable nonhydrostatic atmospheric dycore for the
 1039 energy exascale earth system model running at cloud-resolving resolutions. In
 1040 *2020 SC20: International Conference for High Performance Computing, Net-*
 1041 *working, Storage and Analysis (SC)* (p. 1304-1317). Los Alamitos, CA, USA:
 1042 IEEE Computer Society. doi: 10.1109/SC41405.2020.00096
- 1043 Bodas-Salcedo, A., Williams, K. D., Ringer, M. A., Beau, I., Cole, J. N. S.,
 1044 Dufresne, J.-L., ... Yokohata, T. (2014). Origins of the Solar Radiation
 1045 Biases over the Southern Ocean in CFMIP2 Models. *Journal of Climate*,
 1046 27(1), 41–56. doi: 10.1175/JCLI-D-13-00169.1
- 1047 Bogenschutz, P., & Krueger, S. K. (2013). A simplified pdf parameterization of
 1048 subgrid-scale clouds and turbulence for cloud-resolving models. *Journal of*
 1049 *Advances in Modeling Earth Systems*, 5(2), 195-211. doi: https://doi.org/
 1050 10.1002/jame.20018
- 1051 Bogenschutz, P., Yamaguchi, T., & Lee, H.-H. (2021). "e3sm simulations with high
 1052 vertical resolution in the lower troposphere". (Accepted, J. Adv. Modeling
 1053 Earth Sys.)
- 1054 Boyle, J., & Klein, S. A. (2010). Impact of horizontal resolution on climate
 1055 model forecasts of tropical precipitation and diabatic heating for the twp-
 1056 ice period. *Journal of Geophysical Research: Atmospheres*, 115(D23). doi:
 1057 10.1029/2010JD014262
- 1058 Bradley, A. M., Bosler, P. A., Guba, O., Taylor, M. A., & Barnett, G. A. (2019).
 1059 Communication-efficient property preservation in tracer transport. *SIAM Jour-*
 1060 *nal on Scientific Computing*, 41(3), C161–C193. doi: 10.1137/18m1165414
- 1061 Bretherton, C. S., & Khairoutdinov, M. F. (2015). Convective self-aggregation feed-
 1062 backs in near-global cloud-resolving simulations of an aquaplanet. *Journal of*
 1063 *Advances in Modeling Earth Systems*, 7(4), 1765-1787. doi: https://doi.org/10
 1064 .1002/2015MS000499
- 1065 Bretherton, C. S., & Park, S. (2009). A new moist turbulence parameterization
 1066 in the community atmosphere model. *Journal of Climate*, 22(12), 3422 - 3448.
 1067 doi: 10.1175/2008JCLI2556.1
- 1068 Caldwell, P. M. (2010). California wintertime precipitation bias in regional and
 1069 global climate models. *Journal of Applied Meteorology and Climatology*,
 1070 49(10), 2147 - 2158. doi: 10.1175/2010JAMC2388.1
- 1071 Caldwell, P. M., Mametjanov, A., Tang, Q., Van Roekel, L. P., Golaz, J.-C., Lin,
 1072 W., ... Zhou, T. (2019). The doe e3sm coupled model version 1: Descrip-
 1073 tion and results at high resolution. *Journal of Advances in Modeling Earth*
 1074 *Systems*, 11(12), 4095-4146. doi: https://doi.org/10.1029/2019MS001870
- 1075 Carter-Edwards, H., Trott, C. R., & Sunderland, D. (2014). Kokkos: Enabling
 1076 manycore performance portability through polymorphic memory access pat-
 1077 terns. *J. Parallel and Dist. Comp.*, 74(12), 3202–3216.
- 1078 Cheng, A., & Xu, K.-M. (2008). Simulation of boundary-layer cumulus and strato-
 1079 cumulus clouds using a cloud-resolving model with low-and third-order
 1080 turbulence closures. *Journal of the Meteorological Society of Japan. Ser. II*,
 1081 86A, 67-86. doi: 10.2151/jmsj.86A.67
- 1082 Covey, C., Gleckler, P. J., Doutriaux, C., Williams, D. N., Dai, A., Fasullo, J., ...
 1083 Berg, A. (2016). Metrics for the diurnal cycle of precipitation: Toward routine
 1084 benchmarks for climate models. *Journal of Climate*, 29(12), 4461 - 4471. doi:
 1085 10.1175/JCLI-D-15-0664.1
- 1086 Danabasoglu, G., Lamarque, J.-F., Bacmeister, J., Bailey, D. A., DuVivier, A. K.,
 1087 Edwards, J., ... Strand, W. G. (2020). The community earth system
 1088 model version 2 (cesm2). *Journal of Advances in Modeling Earth Sys-*

- 1089 *tems*, 12(2), e2019MS001916. (e2019MS001916 2019MS001916) doi:
 1090 <https://doi.org/10.1029/2019MS001916>
- 1091 Delworth, T. L., Rosati, A., Anderson, W., Adcroft, A. J., Balaji, V., Benson, R.,
 1092 ... Zhang, R. (2012). Simulated climate and climate change in the gfdl cm2.5
 1093 high-resolution coupled climate model. *Journal of Climate*, 25(8), 2755-2781.
 1094 doi: 10.1175/JCLI-D-11-00316.1
- 1095 Dennis, J., Edwards, J., Evans, K., Guba, O., Lauritzen, P., Mirin, A., ... Worley,
 1096 P. H. (2012). CAM-SE: A scalable spectral element dynamical core for the
 1097 community atmosphere model. *Int. J. High Perf. Comp. Appl.*, 26, 74-89.
- 1098 Dennis, J., Fournier, A., Spatz, W. F., St.-Cyr, A., Taylor, M. A., Thomas, S. J.,
 1099 & Tufo, H. (2005). High resolution mesh convergence properties and parallel
 1100 efficiency of a spectral element atmospheric dynamical core. *Int. J. High Perf.*
 1101 *Comp. Appl.*, 19, 225-235.
- 1102 Dettinger, M. D., Ralph, F. M., Das, T., Neiman, P. J., & Cayan, D. R. (2011). At-
 1103 mospheric Rivers, Floods and the Water Resources of California. *Water*, 3(2),
 1104 445-478. doi: 10.3390/w3020445
- 1105 Doelling, D. R., Loeb, N. G., Keyes, D. F., Nordeen, M. L., Morstad, D., Nguyen,
 1106 C., ... Sun, M. (2013). Geostationary enhanced temporal interpolation for
 1107 ceres flux products. *Journal of Atmospheric and Oceanic Technology*, 30(6),
 1108 1072 - 1090. doi: 10.1175/JTECH-D-12-00136.1
- 1109 Doelling, D. R., Sun, M., Nguyen, L. T., Nordeen, M. L., Haney, C. O., Keyes,
 1110 D. F., & Mlynchak, P. E. (2016). Advances in geostationary-derived longwave
 1111 fluxes for the ceres synoptic (syn1deg) product. *Journal of Atmospheric and*
 1112 *Oceanic Technology*, 33(3), 503 - 521. doi: 10.1175/JTECH-D-15-0147.1
- 1113 Duffy, P. B., Govindasamy, B., Iorio, J. P., Milanovich, J., Sperber, K. R., Taylor,
 1114 K. E., ... Thompson, S. L. (2003). High-resolution simulations of global
 1115 climate, part 1: present climate. *Clim. Dyn.*, 21, 371-390.
- 1116 Edman, J. P., & Romps, D. M. (2014). An improved weak-pressure-gradient scheme
 1117 for single-column modeling. *Journal of the Atmospheric Sciences*, 71(7), 2415-
 1118 2429.
- 1119 Evans, K., Lauritzen, P., Mishra, S., Neale, R., Taylor, M., & Tribbia, J. (2013).
 1120 AMIP simulation with the CAM4 spectral element dynamical core. *J. Climate*,
 1121 26(3), 689-709.
- 1122 Field, P. R., Cotton, R. J., McBeath, K., Lock, A. P., Webster, S., & Allan, R. P.
 1123 (2014). Improving a convection-permitting model simulation of a cold air
 1124 outbreak. *Quarterly Journal of the Royal Meteorological Society*, 140(678),
 1125 124-138.
- 1126 Findeisen, W. (1938). *Kolloid-meteorologische vorgänge bei neiderschlags-bildung*.
 1127 (Vol. 55).
- 1128 Flatau, P. J., Walko, R. L., & Cotton, W. R. (1992). Polynomial fits to saturation
 1129 vapor pressure. *Journal of Applied Meteorology (1988-2005)*, 31(12),
 1130 1507-1513.
- 1131 Fletcher, J., Mason, S., & Jakob, C. (2016). The Climatology, Meteorology, and
 1132 Boundary Layer Structure of Marine Cold Air Outbreaks in Both Hemispheres.
 1133 *Journal of Climate*, 29(6), 1999-2014. doi: 10.1175/JCLI-D-15-0268.1
- 1134 Fosser, G., Khodayar Pardo, S., & Berg, P. (2014). Benefit of convection permitting
 1135 climate model simulations in the representation of convective precipitation.
 1136 *Climate Dynamics*, 44, 45-60. doi: 10.1007/s00382-014-2242-1
- 1137 Gelaro, R., Putman, W. M., Pawson, S., et al. (2015). *Evaluation of the 7-km geos-*
 1138 *5 nature run* (Tech. Rep. Series on Glob. Model Data Assim.) Greenbelt MD,
 1139 USA: NASA.
- 1140 Geleyn, J., & Hollingsworth, A. (1979). An economical analytical method for the
 1141 computation of the interaction between scattering and line absorption of radiation.
 1142 *Beitr. Phys. Atmos.*, 52(1), 1 - 16.
- 1143 Gettelman, A., Liu, X., Ghan, S. J., Morrison, H., Park, S., Conley, A. J., ...

- 1144 Li, J.-L. F. (2010). Global simulations of ice nucleation and ice super-
 1145 saturation with an improved cloud scheme in the community atmosphere
 1146 model. *Journal of Geophysical Research: Atmospheres*, *115*(D18). doi:
 1147 <https://doi.org/10.1029/2009JD013797>
- 1148 Gettelman, A., & Morrison, H. (2015). Advanced two-moment bulk microphysics for
 1149 global models. part i: Off-line tests and comparison with other schemes. *Jour-
 1150 nal of Climate*, *28*(3), 1268 - 1287. doi: 10.1175/JCLI-D-14-00102.1
- 1151 Ghan, S. J., & Zaveri, R. A. (2007). Parameterization of optical properties for
 1152 hydrated internally mixed aerosol. *Journal of Geophysical Research: Atmo-
 1153 spheres*, *112*(D10). doi: <https://doi.org/10.1029/2006JD007927>
- 1154 Giorgi, F., & Marinucci, M. R. (1996). A investigation of the sensitivity of
 1155 simulated precipitation to model resolution and its implications for cli-
 1156 mate studies. *Monthly Weather Review*, *124*(1), 148 - 166. doi: 10.1175/
 1157 1520-0493(1996)124(0148:AIOTSO)2.0.CO;2
- 1158 Godoy, W. F., Podhorszki, N., Wang, R., Atkins, C., Eisenhauer, G., Gu, J., ...
 1159 Klasky, S. (2020). Adios 2: The adaptable input output system. a frame-
 1160 work for high-performance data management. *SoftwareX*, *12*, 100561. doi:
 1161 <https://doi.org/10.1016/j.softx.2020.100561>
- 1162 Golaz, J.-C., Caldwell, P. M., Van Roekel, L. P., Petersen, M. R., Tang, Q., Wolfe,
 1163 J. D., ... Zhu, Q. (2019). The doe e3sm coupled model version 1: Overview
 1164 and evaluation at standard resolution. *Journal of Advances in Modeling Earth
 1165 Systems*, *11*(7), 2089-2129. doi: <https://doi.org/10.1029/2018MS001603>
- 1166 Golaz, J.-C., Larson, V. E., & Cotton, W. R. (2002). A pdf-based model for bound-
 1167 ary layer clouds. part i: Method and model description. *Journal of the Atmo-
 1168 spheric Sciences*, *59*(24), 3540 - 3551. doi: 10.1175/1520-0469(2002)059<3540:
 1169 APBMFB>2.0.CO;2
- 1170 Grabowski, W. W. (2016). Towards global large eddy simulation: Super-
 1171 parameterization revisited. *Journal of the Meteorological Society of Japan.
 1172 Ser. II*, *94*(4), 327-344. doi: 10.2151/jmsj.2016-017
- 1173 Grabowski, W. W., & Smolarkiewicz, P. K. (1999). Crcp: a cloud resolving convec-
 1174 tion parameterization for modeling the tropical convecting atmosphere. *Phys-
 1175 ica D: Nonlinear Phenomena*, *133*(1), 171-178. doi: [https://doi.org/10.1016/
 1176 S0167-2789\(99\)00104-9](https://doi.org/10.1016/S0167-2789(99)00104-9)
- 1177 Guan, B., Molotch, N. P., Waliser, D. E., Fetzer, E. J., & Neiman, P. J. (2010).
 1178 Extreme snowfall events linked to atmospheric rivers and surface air temper-
 1179 ature via satellite measurements. *Geophysical Research Letters*, *37*(20). doi:
 1180 10.1029/2010GL044696
- 1181 Guba, O., Taylor, M., & St.-Cyr, A. (2014). Optimization based limiters for the
 1182 spectral element method. *J. Comput. Phys.*, *267*, 176-195. doi: 10.1016/j.jcp
 1183 .2014.02.029
- 1184 Guba, O., Taylor, M. A., Bradley, A. M., Bosler, P. A., & Steyer, A. (2020). A
 1185 framework to evaluate imex schemes for atmospheric models. *Geoscientific
 1186 Model Development*, *13*(12), 6467-6480. doi: 10.5194/gmd-13-6467-2020
- 1187 Hannah, W., Bradley, A., Guba, O., Tang, Q., Golaz, J.-C., & Wolfe, J. (2021).
 1188 *Separating physics and dynamics grids for improved computational efficiency in
 1189 spectral element earth system models.* (Under review, JAMES)
- 1190 Hartnett, E., & Edwards, J. (2021). The parallelio (pio) c/fortran libraries for scal-
 1191 able hpc performance..
- 1192 Hawcroft, M. K., Shaffrey, L. C., Hodges, K. I., & Dacre, H. F. (2012). How
 1193 much northern hemisphere precipitation is associated with extratropical cy-
 1194 clones? *Geophysical Research Letters*, *39*(24). doi: [https://doi.org/10.1029/
 1195 2012GL053866](https://doi.org/10.1029/2012GL053866)
- 1196 Herrington, A. R., Lauritzen, P. H., Taylor, M. A., Goldhaber, S., Eaton, B. E.,
 1197 Bacmeister, J. T., ... Ullrich, P. A. (2019). Physics-dynamics coupling with
 1198 element-based high-order galerkin methods: Quasi-equal-area physics grid.

- 1199 *Mon. Weath. Rev.*, 147(1), 69 - 84. doi: 10.1175/MWR-D-18-0136.1
- 1200 Hersbach, H., Bell, B., Berrisford, P., Hirahara, S., Horányi, A., Muñoz-Sabater,
1201 J., ... Thépaut, J.-N. (2020). The era5 global reanalysis. *Quarterly*
1202 *Journal of the Royal Meteorological Society*, 146(730), 1999-2049. doi:
1203 <https://doi.org/10.1002/qj.3803>
- 1204 Hewitt, H., Roberts, M., Mathiot, P., Biastoch, A., Blockley, E., Chassignet,
1205 E., ... Zhang, Q. (2020). Resolving and parameterising the ocean
1206 mesoscale in earth system models. *Current Climate Change Reports*. doi:
1207 10.1007/s40641-020-00164-w
- 1208 Hohenegger, C., Kornblueh, L., Klocke, D., Becker, T., Cioni, G., Engels, J. F., ...
1209 Stevens, B. (2020). Climate statistics in global simulations of the atmosphere,
1210 from 80 to 2.5 km grid spacing. *Journal of the Meteorological Society of Japan*.
1211 *Ser. II, adpub*. doi: 10.2151/jmsj.2020-005
- 1212 Hou, A. Y., Kakar, R. K., Neeck, S., Azarbarzin, A. A., Kummerow, C. D., Ko-
1213 jima, M., ... Iguchi, T. (2014). The global precipitation measurement mis-
1214 sion. *Bulletin of the American Meteorological Society*, 95(5), 701 - 722. doi:
1215 10.1175/BAMS-D-13-00164.1
- 1216 Huffman, G., Stocker, E., Bolvin, D., Nelkin, E., & Tan, J. (2019). *GPM IMERG*
1217 *Final Precipitation L3 Half Hourly 0.1 degree x 0.1 degree V06*. (Available
1218 from Goddard Earth Sciences Data and Information Services Center, Accessed
1219 19 March 2020) doi: 10.5067/GPM/IMERG/3B-HH/06
- 1220 Huffman, G. J., & coauthors. (2019). *Nasa global precipitation measurement (gpm)*
1221 *integrated multi-satellite retrievals for gpm (imerg)* (NASA Algorithm Theoret-
1222 ical Basis Doc. No. version 06). Greenbelt MD, USA: NASA.
- 1223 Iorio, J. P., Duffy, P. B., Govindasamy, B., Thompson, S. L., Khairoutdinov, M., &
1224 Randall, D. (2004). Effects of model resolution and subgrid-scale physics on
1225 the simulation of precipitation in the continental United States. *Clim. Dyn.*,
1226 23, 243-258.
- 1227 Jouan, C., Milbrandt, J., Vaillancourt, P., Chosson, F., & Morrison, H. (2020).
1228 Adaptation of the predicted particles properties (p3) microphysics scheme
1229 for large-scale numerical weather prediction. *Weather and Forecasting*, 35,
1230 2541-2565. doi: 10.1175/WAF-D-20-0111.1
- 1231 Judt, F., Klocke, D., Rios-Berrios, R., Vanniere, B., Ziemer, F., Auger, L., ... Zhou,
1232 L. (2021). Tropical Cyclones in Global Storm-Resolving Models. *Journal of the*
1233 *Meteorological Society of Japan. Ser. II, adpub*. doi: 10.2151/jmsj.2021-029
- 1234 Jung, T., Gulev, S. K., Rudeva, I., & Soloviev, V. (2006). Sensitivity of extrat-
1235 ropical cyclone characteristics to horizontal resolution in the ECMWF model.
1236 *Quarterly Journal of the Royal Meteorological Society*, 132(619), 1839-1857.
1237 doi: <https://doi.org/10.1256/qj.05.212>
- 1238 Jung, T., Miller, M. J., Palmer, T. N., Towers, P., Wedi, N., Achuthavarier, D.,
1239 ... Hodges, K. I. (2012). High-resolution global climate simulations with
1240 the ecmwf model in project athena: Experimental design, model climate,
1241 and seasonal forecast skill. *Journal of Climate*, 25(9), 3155-3172. doi:
1242 10.1175/JCLI-D-11-00265.1
- 1243 Kain, J. S., Weiss, S. J., Bright, D. R., Baldwin, M. E., Levit, J. J., Carbin, G. W.,
1244 ... Thomas, K. W. (2008). Some practical considerations regarding horizon-
1245 tal resolution in the first generation of operational convection-allowing nwp.
1246 *Weather and Forecasting*, 23(5), 931 - 952. doi: 10.1175/WAF2007106.1
- 1247 Kasahara, A. (1974). Various vertical coordinate systems used for numerical weather
1248 prediction. *Mon. Weath. Rev.*, 102, 509-522.
- 1249 Kato, S., Sun-Mack, S., Miller, W. F., Rose, F. G., Chen, Y., Minnis, P., & Wielicki,
1250 B. A. (2010). Relationships among cloud occurrence frequency, overlap,
1251 and effective thickness derived from calipso and cloudsat merged cloud verti-
1252 cal profiles. *Journal of Geophysical Research: Atmospheres*, 115(D4). doi:
1253 <https://doi.org/10.1029/2009JD012277>

- 1254 Kendon, E. J., Roberts, N. M., Senior, C. A., & Roberts, M. J. (2012). Realism
1255 of Rainfall in a Very High-Resolution Regional Climate Model. *Journal of Cli-*
1256 *mate*, 25(17), 5791–5806. doi: 10.1175/JCLI-D-11-00562.1
- 1257 Klein, S. A., McCoy, R. B., Morrison, H., Ackerman, A. S., Avramov, A., Boer,
1258 G. d., . . . Zhang, G. (2009). Intercomparison of model simulations of mixed-
1259 phase clouds observed during the arm mixed-phase arctic cloud experiment.
1260 i: single-layer cloud. *Quarterly Journal of the Royal Meteorological Society*,
1261 135(641), 979–1002. doi: <https://doi.org/10.1002/qj.416>
- 1262 Kodama, C., Stevens, B., Mauritsen, T., Seiki, T., & Satoh, M. (2019). A
1263 New Perspective for Future Precipitation Change from Intense Extratrop-
1264 ical Cyclones. *Geophysical Research Letters*, 46(21), 12435–12444. doi:
1265 <https://doi.org/10.1029/2019GL084001>
- 1266 Krueger, S. K., Morrison, H., & Fridlind, A. M. (2016). Cloud-resolving modeling:
1267 Arm and the gcss story. *Meteorological Monographs*, 57, 25.1 - 25.16. doi: 10
1268 .1175/AMSMONOGRAPHS-D-15-0047.1
- 1269 Langhans, W., Schmidli, J., Fuhrer, O., Bieri, S., & Schar, C. (2013). Long-term
1270 simulations of thermally driven flows and orographic convection at convection-
1271 parameterizing and cloud-resolving resolutions. *Journal of Applied Meteorology*
1272 *and Climatology*, 52(6), 1490 - 1510. doi: 10.1175/JAMC-D-12-0167.1
- 1273 Laprise, R. (1992). The Euler equations of motion with hydrostatic pressure as an
1274 independent variable. *Mon. Weath. Rev.*, 120(1), 197–207.
- 1275 Larson, V. E., & Griffin, B. M. (2013). Analytic upscaling of a local microphysics
1276 scheme. part i: Derivation. *Quarterly Journal of the Royal Meteorological Soci-*
1277 *ety*, 139(670), 46–57. doi: <https://doi.org/10.1002/qj.1967>
- 1278 Latham, R., Zingale, M., Thakur, R., Gropp, W., Gallagher, B., Liao, W., . . . Li,
1279 J. (2003). Parallel netcdf: A high-performance scientific i/o interface. In *Sc*
1280 *conference* (p. 39). Los Alamitos, CA, USA: IEEE Computer Society. doi:
1281 10.1109/SC.2003.10053
- 1282 Lauritzen, P. H., Bacmeister, J. T., Callaghan, P. F., & Taylor, M. A. (2015).
1283 Ncar_topo (v1.0): Ncar global model topography generation software for un-
1284 structured grids. *Geoscientific Model Development*, 8(12), 3975–3986. doi:
1285 10.5194/gmd-8-3975-2015
- 1286 Lauritzen, P. H., & Williamson, D. L. (2019). A total energy error analysis of dy-
1287 namical cores and physics-dynamics coupling in the community atmosphere
1288 model (cam). *Journal of Advances in Modeling Earth Systems*, 11(5), 1309-
1289 1328. doi: <https://doi.org/10.1029/2018MS001549>
- 1290 Lavers, D. A., & Villarini, G. (2015). The contribution of atmospheric rivers to pre-
1291 cipitation in Europe and the United States. *Journal of Hydrology*, 522, 382–
1292 390. doi: 10.1016/j.jhydrol.2014.12.010
- 1293 Lebassi-Habtezion, B., & Caldwell, P. M. (2015). Aerosol specification in single-
1294 column community atmosphere model version 5. *Geoscientific Model Develop-*
1295 *ment*, 8(3), 817–828. doi: 10.5194/gmd-8-817-2015
- 1296 Lee, H.-H., Bogenschutz, P., & Yamaguchi, T. (2021). The implementation of
1297 framework for improvement by vertical enhancement (five) into energy exasacle
1298 earth system model (e3sm). *Journal of Advances in Modeling Earth Systems*,
1299 in review.
- 1300 Li, G., & Xie, S.-P. (2014). Tropical biases in cmip5 multimodel ensemble: The ex-
1301 cessive equatorial pacific cold tongue and double itcz problems. *Journal of Cli-*
1302 *mate*, 27(4), 1765 - 1780. doi: 10.1175/JCLI-D-13-00337.1
- 1303 Lin, S.-J. (2004). A vertically Lagrangian finite-volume dynamical core for global
1304 models. *Mon. Weath. Rev.*, 132, 2293–2397.
- 1305 Lindborg, E. (1999). Can the atmospheric kinetic energy spectrum be explained by
1306 two-dimensional turbulence? *Fluid Mech.*, 388, 259–288.
- 1307 Liu, X., Ma, P.-L., Wang, H., Tilmes, S., Singh, B., Easter, R. C., . . . Rasch,
1308 P. J. (2016). Description and evaluation of a new four-mode version of

- 1309 the modal aerosol module (mam4) within version 5.3 of the community at-
 1310 mosphere model. *Geoscientific Model Development*, 9(2), 505–522. doi:
 1311 10.5194/gmd-9-505-2016
- 1312 Love, B. S., Matthews, A. J., & Lister, G. M. S. (2011). The diurnal cycle of pre-
 1313 cipitation over the maritime continent in a high-resolution atmospheric model.
 1314 *Quarterly Journal of the Royal Meteorological Society*, 137(657), 934–947. doi:
 1315 10.1002/qj.809
- 1316 Ma, H.-Y., Chuang, C. C., Klein, S. A., Lo, M.-H., Zhang, Y., Xie, S., ... Phillips,
 1317 T. J. (2015). An improved hindcast approach for evaluation and diagnosis
 1318 of physical processes in global climate models. *J. Adv. Mod. Earth Syst.*, 7,
 1319 1810–1827. doi: <https://doi.org/10.1002/2015MS000490>
- 1320 Madden, R. A., & Julian, P. R. (1971). Detection of a 40–50 day oscillation in the
 1321 zonal wind in the tropical pacific. *Journal of Atmospheric Sciences*, 28(5), 702
 1322 - 708. doi: 10.1175/1520-0469(1971)028<0702:DOADOI>2.0.CO;2
- 1323 Maslowski, W., Clement-Kinney, J., Marble, D., & Jakacki, J. (2008). Towards eddy-
 1324 resolving models of the Arctic Ocean. In M. Hecht & H. Hasumi (Eds.), *Ocean*
 1325 *modeling in an eddying regime* (Vol. 177, pp. 241–264). American Geophysical
 1326 Union.
- 1327 McClean, J. L., Bader, D. C., Bryan, F. O., Maltrud, M. E., Dennis, J. M., Mirin,
 1328 A. A., ... Worley, P. H. (2011). A prototype two-decade fully-coupled
 1329 fine-resolution ccsm simulation. *Ocean Modelling*, 39(1), 10 - 30. (Mod-
 1330 elling and Understanding the Ocean Mesoscale and Submesoscale) doi:
 1331 <https://doi.org/10.1016/j.ocemod.2011.02.011>
- 1332 McClenny, E. E., Ullrich, P. A., & Grotjahn, R. (2020). Sensitivity of atmo-
 1333 spheric river vapor transport and precipitation to uniform sea surface tem-
 1334 perature increases. *Journal of Geophysical Research: Atmospheres*, 125(21),
 1335 e2020JD033421.
- 1336 McCoy, I. L., Wood, R., & Fletcher, J. K. (2017). Identifying Meteorological Con-
 1337 trols on Open and Closed Mesoscale Cellular Convection Associated with
 1338 Marine Cold Air Outbreaks. *Journal of Geophysical Research: Atmospheres*,
 1339 122, 11,678–11,702. doi: <https://doi.org/10.1002/2017JD027031>
- 1340 Milbrandt, J. A., & Morrison, H. (2016). Parameterization of cloud microphysics
 1341 based on the prediction of bulk ice particle properties. part iii: Introduction of
 1342 multiple free categories. *Journal of the Atmospheric Sciences*, 73(3), 975 - 995.
 1343 doi: 10.1175/JAS-D-15-0204.1
- 1344 Mitchell, D. L. (2002). Effective diameter in radiation transfer: General definition,
 1345 applications, and limitations. *Journal of the Atmospheric Sciences*, 59(15),
 1346 2330–2346.
- 1347 Miura, H., Satoh, M., Nasuno, T., Noda, A. T., & Oouchi, K. (2007). A madden-
 1348 julian oscillation event realistically simulated by a global cloud-resolving
 1349 model. *Science*, 318(5857), 1763–1765. doi: 10.1126/science.1148443
- 1350 Miyakawa, T., Satoh, M., Miura, H., Tomita, H., Yashiro, H., Noda, A., ...
 1351 Yoneyama, K. (2014). Madden–julian oscillation prediction skill of a new-
 1352 generation global model demonstrated using a supercomputer. *Nature commu-
 1353 nications*, 5, 3769. doi: 10.1038/ncomms4769
- 1354 Morrison, H., & Gettelman, A. (2008). A new two-moment bulk stratiform cloud
 1355 microphysics scheme in the community atmosphere model, version 3 (cam3).
 1356 part i: Description and numerical tests. *Journal of Climate*, 21(15), 3642 -
 1357 3659. doi: 10.1175/2008JCLI2105.1
- 1358 Morrison, H., & Grabowski, W. W. (2008). Modeling supersaturation and subgrid-
 1359 scale mixing with two-moment bulk warm microphysics. *Journal of the Atmo-
 1360 spheric Sciences*, 65(3), 792 - 812. doi: 10.1175/2007JAS2374.1
- 1361 Morrison, H., & Milbrandt, J. A. (2015). Parameterization of cloud microphysics
 1362 based on the prediction of the bulk ice particle properties. part i: Scheme
 1363 description and idealized tests. *J. Atmos. Sci.*, 72, 287–311.

- 1364 Murphy, D. M., & Koop, T. (2005). Review of the vapour pressures of ice and su-
 1365 percooled water for atmospheric applications. *Quarterly Journal of the Royal*
 1366 *Meteorological Society*, *131*(608), 1539-1565. doi: <https://doi.org/10.1256/qj.04>
 1367 .94
- 1368 Nam, C., Bony, S., Dufresne, J.-L., & Chepfer, H. (2012). The ‘too few, too bright’
 1369 tropical low-cloud problem in cmip5 models. *Geophysical Research Letters*,
 1370 *39*(21). doi: <https://doi.org/10.1029/2012GL053421>
- 1371 Narenpitak, P., Bretherton, C. S., & Khairoutdinov, M. F. (2017). Cloud and circula-
 1372 tion feedbacks in a near-global aquaplanet cloud-resolving model. *Journal of*
 1373 *Advances in Modeling Earth Systems*, *9*(2), 1069-1090. doi: <https://doi.org/10>
 1374 .1002/2016MS000872
- 1375 Nastrom, G., & Gage, K. S. (1985). A climatology of atmospheric wavenumber spec-
 1376 tra of wind and temperature observed by commercial aircraft. *J. Atmos. Sci.*,
 1377 *42*, 950–960.
- 1378 Neale, R. B., Gettelman, A., Park, S., Chen, C.-C., Lauritzen, P. H., Williamson,
 1379 D. L., ... Taylor, M. A. (2012). *Description of the NCAR Community Atmo-*
 1380 *sphere Model (CAM 5.0)* (NCAR Technical Note Nos. TN-486+STR). Boulder
 1381 CO USA: NCAR.
- 1382 Neumann, P., Düben, P., Adamidis, P., Bauer, P., Brueck, M., Kornblueh, L.,
 1383 ... Biercamp, J. (2019). Assessing the scales in numerical weather and
 1384 climate predictions: Will exascale be the rescue? *Philosophical transac-*
 1385 *tions. Series A, Mathematical, physical, and engineering sciences*, *377*. doi:
 1386 10.1098/rsta.2018.0148
- 1387 Ogura, Y. (1963). The evolution of a moist convective element in a shallow, condi-
 1388 tionally unstable atmosphere: A numerical calculation. *Journal of Atmospheric*
 1389 *Sciences*, *20*(5), 407 - 424. doi: 10.1175/1520-0469(1963)020<0407:TEOAMC>2
 1390 .0.CO;2
- 1391 Pfahl, S., & Wernli, H. (2012). Quantifying the Relevance of Cyclones for Precipita-
 1392 tion Extremes. *Journal of Climate*, *25*(19), 6770–6780. doi: 10.1175/JCLI-D
 1393 -11-00705.1
- 1394 Phillips, T. J., Potter, G. L., Williamson, D. L., Cederwall, R. T., Boyle, J. S., Fior-
 1395 ino, M., ... Yio, J. J. (2004). Evaluating parameterizations in general circula-
 1396 tion models: Climate simulation meet with weather prediction. *Bull. Amer.*
 1397 *Meteor. Soc.*, *85*, 1903-1915. doi: <https://doi.org/10.1175/BAMS-85-12-1903>
- 1398 Pincus, R., Barker, H. W., & Morcrette, J.-J. (2003). A fast, flexible, approx-
 1399 imate technique for computing radiative transfer in inhomogeneous cloud
 1400 fields. *Journal of Geophysical Research: Atmospheres*, *108*(D13). doi:
 1401 <https://doi.org/10.1029/2002JD003322>
- 1402 Pincus, R., Mlawer, E. J., & Delamere, J. S. (2019). Balancing accuracy, efficiency,
 1403 and flexibility in radiation calculations for dynamical models. *Journal of Ad-*
 1404 *vances in Modeling Earth Systems*, *11*(10), 3074-3089. doi: <https://doi.org/10>
 1405 .1029/2019MS001621
- 1406 Pope, V. D., & Stratton, R. A. (2002). The processes governing horizontal resolution
 1407 sensitivity in a climate model. *Clim. Dyn.*, *19*, 211-236.
- 1408 Prein, A. F., Gobiet, A., Suklitsch, M., Truhetz, H., Awan, N. K., Keuler, K.,
 1409 & Georgievski, G. (2013). Added value of convection permitting sea-
 1410 sonal simulations. *Climate Dynamics*, *41*(9-10), 2655-2677. doi: 10.1007/
 1411 s00382-013-1744-6
- 1412 Prein, A. F., Langhans, W., Fosse, G., Ferrone, A., Ban, N., Goergen, K., ... Le-
 1413 ung, R. (2015). A review on regional convection-permitting climate modeling:
 1414 Demonstrations, prospects, and challenges. *Reviews of Geophysics*, *53*(2),
 1415 323-361. doi: <https://doi.org/10.1002/2014RG000475>
- 1416 Putman, W. M., & Suarez, M. (2011). Cloud-system resolving simulations with
 1417 the nasa goddard earth observing system global atmospheric model (geos-
 1418 5). *Geophysical Research Letters*, *38*(16). doi: <https://doi.org/10.1029/>

- 1419 2011GL048438
- 1420 Randall, D., Khairoutdinov, M., Arakawa, A., & Grabowski, W. (2003). Breaking
- 1421 the cloud parameterization deadlock. *Bulletin of the American Meteorological*
- 1422 *Society*, *84*(11), 1547 - 1564. doi: 10.1175/BAMS-84-11-1547
- 1423 Rasch, P. J., Xie, S., Ma, P.-L., Lin, W., Wang, H., Tang, Q., . . . Shrivastava, M.
- 1424 (2019). An overview of the atmospheric component of the Energy Exascale
- 1425 Earth System Model. *J. Adv. Model. Earth Sys.*, *11*(8), 2377–2411. doi:
- 1426 10.1029/2019ms001629
- 1427 Reynolds, R. W., Rayner, N. A., Smith, T. M., Stokes, D. C., & Wang, W. (2002).
- 1428 An improved in situ and satellite sst analysis for climate. *J. Climate*, *15*, 1609-
- 1429 1625. doi: [https://doi.org/10.1175/1520-0442\(2002\)015\(1609:AIISAS\)2.0.CO;](https://doi.org/10.1175/1520-0442(2002)015(1609:AIISAS)2.0.CO;2)
- 1430 [2](https://doi.org/10.1175/1520-0442(2002)015(1609:AIISAS)2.0.CO;2)
- 1431 Riehl, M., & Malkus, J. (1958). On the heat balance of the equatorial trough. *Geo-*
- 1432 *physica (Helsinki)*, *6*, 503-538.
- 1433 Rutz, J. J., Shields, C. A., Lora, J. M., Payne, A. E., Guan, B., Ullrich, P., . . . oth-
- 1434 ers (2019). The atmospheric river tracking method intercomparison project
- 1435 (artmip): quantifying uncertainties in atmospheric river climatology. *Journal*
- 1436 *of Geophysical Research: Atmospheres*, *124*(24), 13777–13802.
- 1437 Rémillard, J., & Tselioudis, G. (2015). Cloud Regime Variability over the Azores
- 1438 and Its Application to Climate Model Evaluation. *J. Climate*, *28*(24), 9707–
- 1439 9720. doi: 10.1175/JCLI-D-15-0066.1
- 1440 Sanders, F., & Gyakum, J. R. (1980). Synoptic-Dynamic Climatology of the
- 1441 “Bomb”. *Monthly Weather Review*, *108*(10), 1589–1606. doi: 10.1175/
- 1442 1520-0493(1980)108(1589:SDCOT)2.0.CO;2
- 1443 Sanderson, B., Piani, C., Ingram, W., Stone, D., & Allen, M. R. (2008). Towards
- 1444 constraining climate sensitivity by linear analysis of feedback patterns in thou-
- 1445 sands of perturbed-physics gcm simulations. *Clim. Dyn.*, *30*, 175–190. doi:
- 1446 10.1007/s00382-007-0280-7
- 1447 Santos, S. P., Bretherton, C., & Caldwell, P. (2020). Cloud process coupling and
- 1448 time integration in the e3sm atmosphere model. *Earth and Space Science Open*
- 1449 *Archive*, *34*. (In review at JAMES) doi: 10.1002/essoar.10504538.2
- 1450 Satoh, M. (2002). Conservative scheme for the compressible nonhydrostatic models
- 1451 with the horizontally explicit and vertically implicit time integration scheme.
- 1452 *Mon. Weath. Rev.*, *130*, 1227–1245.
- 1453 Satoh, M., Matsuno, T., Tomita, H., Miura, H., Nasuno, T., & Iga, S. (2008). Non-
- 1454 hydrostatic icosahedral atmospheric model (nicam) for global cloud resolving
- 1455 simulations. *Journal of Computational Physics*, *227*(7), 3486-3514. (Pre-
- 1456 dicting weather, climate and extreme events) doi: [https://doi.org/10.1016/](https://doi.org/10.1016/j.jcp.2007.02.006)
- 1457 [j.jcp.2007.02.006](https://doi.org/10.1016/j.jcp.2007.02.006)
- 1458 Satoh, M., Stevens, B., Judt, F., Khairoutdinov, M., Lin, S.-J., Putman, W. M., &
- 1459 Duben, P. (2019). Global cloud-resolving models. *Curr Clim Change Rep*, *5*,
- 1460 172-184. doi: <https://doi.org/10.1007/s40641-019-00131-0>
- 1461 Satoh, M., Tomita, H., Yashiro, H., Miura, H., Kodama, C., Seiki, T., . . .
- 1462 Kubokawa, H. (2014). The non-hydrostatic icosahedral atmospheric model:
- 1463 description and development. *Progress in Earth and Planetary Science*, *1*, 18.
- 1464 doi: 10.1186/s40645-014-0018-1
- 1465 Schwartz, C. S., Kain, J. S., Weiss, S. J., Xue, M., Bright, D. R., Kong, F., . . .
- 1466 Coniglio, M. C. (2009). Next-day convection-allowing wrf model guidance:
- 1467 A second look at 2-km versus 4-km grid spacing. *Monthly Weather Review*,
- 1468 *137*(10), 3351 - 3372. doi: 10.1175/2009MWR2924.1
- 1469 Shapiro, M. A., Fedor, L. S., & Hampel, T. (1987). Research aircraft measure-
- 1470 ments of a polar low over the Norwegian Sea. *Tellus A*, *39A*(4), 272–306. doi:
- 1471 <https://doi.org/10.1111/j.1600-0870.1987.tb00309.x>
- 1472 Sherwood, S., Bony, S., & Dufresne, J. (2014). Spread in model climate sensitivity
- 1473 traced to atmospheric convective mixing. *Nature*, *505*, 37-42. doi: 10.1038/

- 1474 nature12829
 1475 Shi, X., & Liu, X. (2018). Sensitivity study of anthropogenic aerosol indirect forcing
 1476 through cirrus clouds with cam5 using three ice nucleation parameterizations.
 1477 *Journal of Meteorological Research*, *32*(qxxbywb-32-5-shixiangjun), 693. doi:
 1478 10.1007/s13351-018-8011-z
- 1479 Simmons, A. J., & Burridge, D. M. (1981). An energy and angular momentum con-
 1480 serving vertical finite-difference scheme and hybrid vertical coordinates. *Mon.*
 1481 *Weath. Rev.*, *109*, 758–766.
- 1482 Skamarock, W. C., Klemp, J. B., Dudhia, J., Gill, D. O., Liu, Z., Berner, J., ...
 1483 Huang, X.-Y. (2019). *A Description of the Advanced Research WRF Version 4*
 1484 (Tech. Rep.). Boulder CO, USA: NCAR Tech. Note NCAR/TN-556+STR.
- 1485 Small, R. J., Bacmeister, J., Bailey, D., Baker, A., Bishop, S., Bryan, F., ... Verten-
 1486 stein, M. (2014). A new synoptic scale resolving global climate simulation
 1487 using the Community Earth System Model. *Journal of Advances in Modeling*
 1488 *Earth Systems*, *6*(4), 1065–1094. doi: 10.1002/2014ms000363
- 1489 Song, X., & Zhang, G. J. (2011). Microphysics parameterization for convective
 1490 clouds in a global climate model: Description and single-column model
 1491 tests. *Journal of Geophysical Research: Atmospheres*, *116*(D2). doi:
 1492 <https://doi.org/10.1029/2010JD014833>
- 1493 Stephens, G. L., L'Ecuyer, T., Forbes, R., Gettelmen, A., Golaz, J.-C., Bodas-
 1494 Salcedo, A., ... Haynes, J. (2010). Dreary state of precipitation in global
 1495 models. *Journal of Geophysical Research: Atmospheres*, *115*(D24). doi:
 1496 <https://doi.org/10.1029/2010JD014532>
- 1497 Stevens, B., & Bony, S. (2013). What are climate models missing? *Science*,
 1498 *340*(6136), 1053–1054. doi: 10.1126/science.1237554
- 1499 Stevens, B., Satoh, M., Auger, L., Biercamp, J., Bretherton, C. S., Chen, X., ...
 1500 Zhou, L. (2019). DYAMOND: the Dynamics of the Atmospheric general circu-
 1501 lation Modeled On Non-hydrostatic Domains. *Progress in Earth and Planetary*
 1502 *Science*, *6*(1), 61. doi: 10.1186/s40645-019-0304-z
- 1503 Steyer, A., Vogl, C. J., Taylor, M., & Guba, O. (2019). Efficient IMEX Runge-Kutta
 1504 methods for nonhydrostatic dynamics. *arXiv e-prints*, arXiv:1906.07219.
- 1505 Storer, R. L., Zhang, G. J., & Song, X. (2015). Effects of convective microphysics
 1506 parameterization on large-scale cloud hydrological cycle and radiative budget
 1507 in tropical and midlatitude convective regions. *Journal of Climate*, *28*(23),
 1508 9277 - 9297. doi: 10.1175/JCLI-D-15-0064.1
- 1509 Su, H., Jiang, J. H., Teixeira, J., Gettelman, A., Huang, X., Stephens, G., ... Pe-
 1510 run, V. S. (2011). Comparison of regime-sorted tropical cloud profiles ob-
 1511 served by cloudsat with geos5 analyses and two general circulation model
 1512 simulations. *Journal of Geophysical Research: Atmospheres*, *116*(D9). doi:
 1513 <https://doi.org/10.1029/2010JD014971>
- 1514 Taylor, M. A., & Fournier, A. (2010). A compatible and conservative spectral ele-
 1515 ment method on unstructured grids. *J. Comput. Phys.*, *229*, 5879– 5895. doi:
 1516 10.1016/j.jcp.2010.04.008
- 1517 Taylor, M. A., Guba, O., Steyer, A., Ullrich, P. A., Hall, D. M., & Eldrid, C. (2020).
 1518 An energy consistent discretization of the nonhydrostatic equations in prim-
 1519 itive variables. *Journal of Advances in Modeling Earth Systems*, *12*(1). doi:
 1520 10.1029/2019MS001783
- 1521 Terai, C. R., Caldwell, P. M., Klein, S. A., Tang, Q., & Branstetter, M. L. (2018).
 1522 The atmospheric hydrologic cycle in the acme v0.3 model. *Climate Dynamics*,
 1523 *50*(9), 3251–3279. doi: 10.1007/s00382-017-3803-x
- 1524 Terpstra, A., Michel, C., & Spengler, T. (2016). Forward and Reverse Shear En-
 1525 vironments during Polar Low Genesis over the Northeast Atlantic. *Monthly*
 1526 *Weather Review*, *144*(4), 1341–1354. doi: 10.1175/MWR-D-15-0314.1
- 1527 Tomita, H., Miura, H., Iga, S., Nasuno, T., & Satoh, M. (2005). A global cloud-
 1528 resolving simulation: Preliminary results from an aqua planet experiment.

- 1529 *Geophysical Research Letters*, 32(8).
- 1530 Ullrich, P. A., & Zarzycki, C. M. (2017). Tempestextremes: A framework for scale-
1531 insensitive pointwise feature tracking on unstructured grids. *Geoscientific*
1532 *Model Development*, 10(3), 1069.
- 1533 Viovy, N. (2018). *Crunccep version 7 - atmospheric forcing data for the community*
1534 *land model*. Boulder CO: Research Data Archive at the National Center for
1535 Atmospheric Research, Computational and Information Systems Laboratory.
- 1536 Wegener, A. (1911). *Thermodynamik der atmosphäre*.
- 1537 Wehner, M. F., Reed, K. A., Li, F., Prabhat, Bacmeister, J., Chen, C.-T., ...
1538 Jablonowski, C. (2014). The effect of horizontal resolution on simulation
1539 quality in the Community Atmospheric Model, CAM5.1. *Journal of Advances*
1540 *in Modeling Earth Systems*, 6(4), 980-997. doi: 10.1002/2013MS000276
- 1541 Weisman, M. L., Skamarock, W. C., & Klemp, J. B. (1997). The resolution de-
1542 pendence of explicitly modeled convective systems. *Monthly Weather Review*,
1543 125(4), 527 - 548. doi: 10.1175/1520-0493(1997)125(0527:TRDOEM)2.0.CO;2
- 1544 Williamson, D. L., Olson, J. G., Hannay, C., Toniazzo, T., Taylor, M., & Yudin,
1545 V. (2015). Energy considerations in the community atmosphere model
1546 (cam). *Journal of Advances in Modeling Earth Systems*, 7(3), 1178-1188.
1547 doi: <https://doi.org/10.1002/2015MS000448>
- 1548 Wiscombe, W. J. (1996). *Mie scattering calculations: Advances in technique and*
1549 *fast, vector-speed computer codes* (NCAR Technical Note Nos. TN-140+STR).
1550 Boulder CO, USA: NCAR.
- 1551 Yin, L., Fu, R., Shevliakova, E., & Dickinson, R. (2012). How well can cmip5 sim-
1552 ulate precipitation and its controlling processes over tropical south america?
1553 *Climate Dynamics*, 41. doi: 10.1007/s00382-012-1582-y
- 1554 Zarzycki, C. M., & Jablonowski, C. (2015). Experimental tropical cyclone forecasts
1555 using a variable-resolution global model. *Monthly Weather Review*, 143(10),
1556 4012-4037.
- 1557 Zarzycki, C. M., Thatcher, D. R., & Jablonowski, C. (2017). Objective tropical
1558 cyclone extratropical transition detection in high-resolution reanalysis and
1559 climate model data. *Journal of Advances in Modeling Earth Systems*, 9(1),
1560 130-148.
- 1561 Zhang, K., Liu, X., Yoon, J.-H., Wang, M., Comstock, J. M., Barahona, D., &
1562 Kooperman, G. (2013). Assessing aerosol indirect effect through ice clouds in
1563 cam5. *AIP Conference Proceedings*, 1527(1), 751-751. doi: 10.1063/1.4803379
- 1564 Zhang, S., Fu, H., Wu, L., Li, Y., Wang, H., Zeng, Y., ... Guo, Y. (2020). Opti-
1565 mizing high-resolution Community Earth System Model on a Heterogeneous
1566 Many-Core Supercomputing Platform (CESM-HR_SW1.0). *Geoscientific Model*
1567 *Development Discussions*, 2020, 1-38. doi: 10.5194/gmd-2020-18
- 1568 Zheng, X., Klein, S., Ghate, V., Santos, S., Mcgibbon, J., Caldwell, P., ... Cadeddu,
1569 M. (2020). Assessment of Precipitating Marine Stratocumulus Clouds in
1570 the E3SMv1 Atmosphere Model: A Case Study from the ARM MAGIC Field
1571 Campaign. *Monthly Weather Review*, 148. doi: 10.1175/MWR-D-19-0349.1
- 1572 Zhu, Y., & Newell, R. E. (1998). A Proposed Algorithm for Moisture Fluxes from
1573 Atmospheric Rivers. *Monthly Weather Review*, 126(3), 725-735. doi: 10.1175/
1574 1520-0493(1998)126(0725:APAFMF)2.0.CO;2